From imaging to material identification: A generalized concept of topological sensitivity

Bojan B. Guzina*, Ivan Chikichev

Department of Civil Engineering, University of Minnesota, Minneapolis, MN 55455, USA

Abstract

To establish a compact analytical framework for the preliminary stress-wave identification of material defects, the focus of this study is an extension of the concept of topological derivative, rooted in elastostatics and the idea of cavity nucleation, to 3D elastodynamics involving germination of solid obstacles. The main result of the proposed generalization is an expression for topological sensitivity, explicit in terms of the elastodynamic Green's function, obtained by an asymptotic expansion of a misfit-type cost functional with respect to the nucleation of a dissimilar elastic inclusion in a defect-free "reference" solid. The featured formula, consisting of an inertial-contrast monopole term and an elasticity-contrast dipole term, is shown to be applicable to a variety of reference solids (semi-infinite and infinite domains with constant or functionally graded elastic properties) for which the Green's functions are available. To deal with situations when the latter is not the case (e.g. finite reference bodies or those with pre-existing defects), an adjoint field approach is employed to derive an alternative expression for topological sensitivity that involves the contraction of two (numerically computed) elastodynamic states. A set of numerical results is included to demonstrate the potential of generalized topological derivative as an efficient tool for exposing not only the geometry, but also material characteristics of subsurface material defects through a local, *point-wise* identification of "optimal" inclusion properties that minimize the topological sensitivity at sampling location. Beyond the realm of non-invasive characterization of engineered materials, the proposed developments may be relevant to medical diagnosis and in particular to breast cancer detection where focused ultrasound waves show a promise of superseding manual palpation.
© 2006 Elsevier Ltd. All rights reserved.

Keywords: Inverse scattering; Elastic waves; Topological sensitivity; Imaging; Transmission problem

*Corresponding author. Tel.: +1 612 626 0789; fax: +1 612 626 7750.
E-mail address: guzina@wave.ce.umn.edu (B.B. Guzina).

1. Introduction

Elastic-wave identification of defects and heterogeneities embedded in semi-infinite or finite bodies is a problem of considerable interest in mechanics owing to its applications in material characterization, seismology, and medical diagnosis. The underlying inverse solutions can be derived from a variety of computational platforms that include e.g. (far-field) ray theory (Aki and Richards, 2002), finite-difference approximation of the wave equation (Sheriff and Geldart, 1995; Schroeder et al., 2002), and boundary integral formulations (Bonnet, 1995). In the context of 3D material characterization, these approaches carry a substantial computational cost associated with solving the forward problem. This precludes the use of global search techniques such as genetic algorithms which involve a large number of forward simulations. To mitigate the problem, gradient-based optimization algorithms have been proposed as a computationally tractable alternative to solving inverse scattering problems, especially when aided by the analytical gradient estimates (Plessix et al., 1998; Guzina and Bonnet, 2004). Unfortunately, the latter class of solutions necessitate a reliable preliminary information about the geometry and material characteristics of hidden defects for satisfactory performance.

Building on the results in shape optimization obtained for Laplace (Sokolowski and Zochowski, 1999; Garreau et al., 2001) and Helmholtz (Samet et al., 2004; Pommier and Samet, 2005) systems, Guzina and Bonnet (2004), Bonnet and Guzina (2004), and Gallego and Rus (2004) have recently established the method of *topological sensitivity* as a tool for preliminary, grid-based reconstruction of obstacles in the context of inverse elastic scattering that requires no prior information (or assumptions in the absence thereof) about the location and geometry of internal defects. In the approach the topological derivative, which quantifies the sensitivity of a given cost functional with respect to the nucleation of an infinitesimal obstacle in the reference (background) medium, is used as an effective obstacle indicator through an assembly of sampling points where it attains pronounced negative values. Typically, the formulas for topological sensitivity permit an explicit representation (e.g. in terms of the Green's function) that is responsible for the computational efficiency of this class of reconstruction techniques. Notwithstanding their usefulness, however, the foregoing analyses are limited in the sense that they are focused on the nucleation of impenetrable scatterers, and in particular *cavities* in 3D (Guzina and Bonnet, 2004; Bonnet and Guzina, 2004) and/or cracks in 2D (Gallego and Rus, 2004) elastodynamics.

In this study, the concept of topological sensitivity is generalized to permit the nucleation of dissimilar *solid inclusions* and thus allow for preliminary elastic-wave identification of subsurface defects of more general nature. On employing a boundary integral approach to derive the necessary asymptotics in terms of the vanishing defect size, it is shown that the proposed generalization (termed "material-topological" sensitivity) consists of a monopole term, related to the mass density contrast, and a dipole term involving the elasticity contrast between the defect and the matrix. To cater for engineering applications, explicit formulas are derived for canonical cases when the nucleating inclusion takes spherical or ellipsoidal shape. For generality, the proposed developments are recast within an alternative framework of the adjoint-field formulation that permits nucleation of inclusions in an arbitrary (infinite or finite, homogeneous or heterogeneous) reference solid. Through numerical examples it is shown that the material-topological sensitivity can be used, in the context of inverse scattering, as an effective defect indicator

through an assembly of sampling points where it attains marked negative values. On varying the material characteristics of the nucleating obstacle, it is also shown that the featured sensitivity can be used as a preparatory tool for *both* geometric and material identification of internal defects.

Beyond their intrinsic potential for the study of localized damage evolution in natural and engineered materials (e.g. Mazars et al., 1991; Xu, 2004; Bonamy et al., 2005), the proposed developments be especially useful in breast cancer detection wherein the knowledge of the shear modulus of a lesion, (geometrically) identified via ultrasound or magnetic resonance imaging, may permit reliable differentiation between the malignant and benign growths (Sarvazyan et al., 1998; Fatemi and Greenleaf, 1998). For completeness, it is noted that the underlying idea of a nucleating inclusion, explored in this study, is similar in spirit to the recent work in Ammari and Kang (2004) dealing with Laplace, elastostatic and Helmholtz systems. Notwithstanding the apparent commonalities, however, the asymptotic expansion methodology, formulas for the generalized topological sensitivity, and the material-geometric identification approach proposed herein have not been established elsewhere.

2. Preliminaries

Consider the inverse scattering problem where the semi-infinite solid, probed by elastic waves, contains a bonded defect Δ_{true} with smooth boundary $\Gamma_{\text{true}} = \partial\Delta_{\text{true}}$ (see Fig. 1). With the Cartesian frame $\{O; \xi_1, \xi_2, \xi_3\}$ set at the top surface Σ, the reference elastic half-space $\Omega = \{(\xi_1, \xi_2, \xi_3) \,|\, \xi_3 > 0\}$ with closure $\bar{\Omega} = \Omega \cup \Sigma$ is characterized by the shear modulus μ, Poisson's ratio v, and mass density ρ. Elastic parameters of the obstacle, $\Delta_{\text{true}} \subset \Omega$, are $\mu^{\star}_{\text{true}}$ and $v^{\star}_{\text{true}}$; its mass density is denoted as $\rho^{\star}_{\text{true}}$. Without loss of generality, it is assumed that the defect is illuminated by a time-harmonic body force distribution $\boldsymbol{f}$ (carrying an implicit time factor $e^{i\omega t}$) whose support and frequency of excitation are denoted by $V_{\text{f}} \subset \Omega$ and ω, respectively. For identification purposes, the induced motion ($\boldsymbol{u}^{\text{obs}}$) is monitored over a finite measurement surface $\Pi^{\text{obs}} = \Pi^{\text{obs}}_{\Sigma} \cup \Pi^{\text{obs}}_{\Omega}$, where $\Pi^{\text{obs}}_{\Sigma} = \Pi^{\text{obs}} \cap \Sigma$ and $\Pi^{\text{obs}}_{\Omega} = \Pi^{\text{obs}} \cap \Omega$ denote its boundary and interior segments, respectively. In the context of medical imaging applications, introduction of the latter segment ($\Pi^{\text{obs}}_{\Omega}$) is motivated by the emergence of the so-called vibro-acustography techniques (Fatemi and
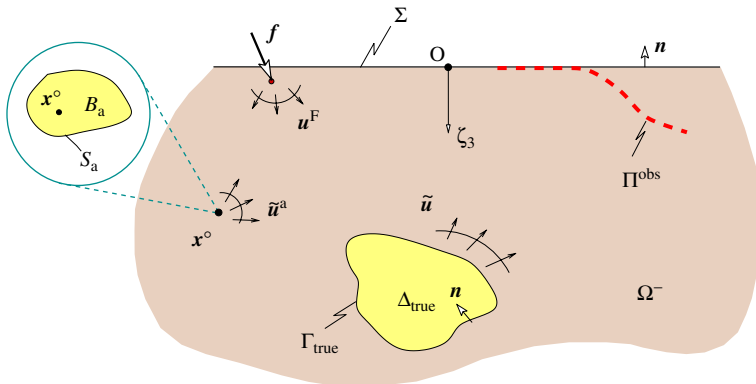

Fig. 1. Illumination of a hidden defect (Δ_{true}) by elastic waves.

Greenleaf, 1998) that entail accurate monitoring of subcutaneous tissue displacement using focused ultrasound beams.

To deal with the defect identification problem depicted in Fig. 1, it is useful to introduce a misfit-type cost functional involving experimental observations $\boldsymbol{u}^{\mathrm{obs}} = \boldsymbol{u}^{\mathrm{obs}}(\boldsymbol{\xi})$ and their elastodynamic predictions $\boldsymbol{u} = \boldsymbol{u}(\boldsymbol{\xi})$ over Π^{obs} so that

$$\mathscr{J}(\Omega^-, \boldsymbol{m}; \boldsymbol{f}) = \int_{\Pi^{\mathrm{obs}}} \varphi(\boldsymbol{u}, \boldsymbol{u}^{\mathrm{obs}}) \, \mathrm{d}\Pi_\xi, \tag{1}$$

where φ is a measure of distance in $\mathbb{R}^3$, assumed to be smooth function of its arguments; $\Omega^- = \Omega \backslash \bar{\Delta}$; $\boldsymbol{m} = (\mu^\star, v^\star, \rho^\star)$ and $\bar{\Delta} = \Delta \cup \Gamma$ signify, respectively, the material properties and closure of a *trial* inclusion Δ bounded by the closed smooth surface Γ, and $\boldsymbol{u}$ is the time-harmonic displacement field which solves the forward scattering problem in the exterior domain (so-called "matrix") Ω^-. To facilitate the ensuing discussion, let $\boldsymbol{I}_k$ denote the symmetric kth-order identity tensor (Dahlquist and Bjorck, 1974), and let $\boldsymbol{C}$ and $\boldsymbol{C}^\star$ be the respective (isotropic) elasticity tensors of the matrix and the inclusion so that

$$\boldsymbol{C} = 3\varkappa \boldsymbol{E}_1 + 2\mu \boldsymbol{E}_2, \quad \boldsymbol{C}^\star = 3\varkappa^\star \boldsymbol{E}_1 + 2\mu^\star \boldsymbol{E}_2, \tag{2}$$

where $\boldsymbol{E}_1 = \frac{1}{3}\boldsymbol{I}_2 \otimes \boldsymbol{I}_2$, $\boldsymbol{E}_2 = \boldsymbol{I}_4 - \boldsymbol{E}_1$, and

$$\varkappa = \frac{2\mu(1+v)}{3(1-2v)}, \quad \varkappa^\star = \frac{2\mu^\star(1+v^\star)}{3(1-2v^\star)}, \tag{3}$$

are the corresponding bulk moduli. With such definitions, $\boldsymbol{u}$ can be shown to solve the field equations

$$\nabla \cdot (\boldsymbol{C} : \nabla \boldsymbol{u}) + \boldsymbol{f} = -\rho \omega^2 \boldsymbol{u}, \quad \boldsymbol{\xi} \in \Omega^-, \tag{4}$$

subject to the boundary and continuity conditions

$$\boldsymbol{t} = 0, \quad \boldsymbol{\xi} \in \Sigma,$$
$$\boldsymbol{u} = \overset{\star}{\boldsymbol{u}}, \quad \boldsymbol{t} = -\overset{\star}{\boldsymbol{t}}, \quad \boldsymbol{\xi} \in \Gamma. \tag{5}$$

Here "$\otimes$" and "$:$" denote, respectively, the usual tensor product and double tensor contraction following the Gibbs dyadic notation (Malvern, 1969); $\overset{\star}{\boldsymbol{u}}$ is the elastodynamic displacement field inside the scatterer, i.e.

$$\nabla \cdot (\boldsymbol{C}^\star : \nabla \overset{\star}{\boldsymbol{u}}) = -\rho^\star \omega^2 \overset{\star}{\boldsymbol{u}}, \quad \boldsymbol{\xi} \in \Delta, \tag{6}$$

and

$$\boldsymbol{t} = \boldsymbol{n} \cdot \boldsymbol{C} : \nabla \boldsymbol{u}, \quad \boldsymbol{\xi} \in \Gamma \cup \Sigma,$$
$$\overset{\star}{\boldsymbol{t}} = \boldsymbol{n}^\star \cdot \boldsymbol{C}^\star : \nabla \overset{\star}{\boldsymbol{u}}, \quad \boldsymbol{n}^\star = -\boldsymbol{n}, \quad \boldsymbol{\xi} \in \Gamma \tag{7}$$

signify, respectively, the surface tractions acting on the matrix with outward normal $\boldsymbol{n}$ and the obstacle whose outward normal is denoted by $\boldsymbol{n}^\star$.

In what follows, it is assumed that $\boldsymbol{u}$ meets the standard continuity requirements for smooth bounding surfaces, i.e. $\boldsymbol{u} \in C^2(\Omega^-) \cap C^1(\bar{\Omega}^-)$ where $\bar{\Omega}^- = \Omega^- \cup \Gamma \cup \Sigma$. For this class of elastic scattering problems, it can be shown (Bonnet, 1999) that the displacement

field in Ω^- satisfies the Somigliana-type integral representation

$$
\boldsymbol{u}(\boldsymbol{x}) = -\boldsymbol{e}_k \int_\Gamma \boldsymbol{u}(\boldsymbol{\xi}) \cdot \hat{\boldsymbol{t}}^k(\boldsymbol{\xi}, \boldsymbol{x}) \, \mathrm{d}\Gamma_\xi + \boldsymbol{e}_k \int_\Gamma \boldsymbol{t}(\boldsymbol{\xi}) \cdot \hat{\boldsymbol{u}}^k(\boldsymbol{\xi}, \boldsymbol{x}) \, \mathrm{d}\Gamma_\xi
$$

$$
+ \boldsymbol{e}_k \int_{V_{\mathrm{f}}} \boldsymbol{f}(\boldsymbol{\xi}) \cdot \hat{\boldsymbol{u}}^k(\boldsymbol{\xi}, \boldsymbol{x}) \, \mathrm{d}\Omega_\xi, \quad \boldsymbol{x} \in \Omega^-. \tag{8}
$$

Here, Einstein summation convention is assumed over the spatial coordinate index $k \in \{1, 2, 3\}$; $\boldsymbol{u}$ satisfies the generalized radiation condition

$$
\lim_{R \to \infty} \int_{\Gamma_R} \{\hat{\boldsymbol{u}}^k(\boldsymbol{\xi}, \boldsymbol{x}) \cdot \boldsymbol{t}(\boldsymbol{\xi}) - \hat{\boldsymbol{t}}^k(\boldsymbol{\xi}, \boldsymbol{x}) \cdot \boldsymbol{u}(\boldsymbol{\xi})\} \, \mathrm{d}\Gamma_\xi = 0, \quad \boldsymbol{x} \in \Omega^-, \; k = 1, 2, 3, \tag{9}
$$

where $\Gamma_R \subset \Omega$ is a hemisphere centered at the origin (Madyarov and Guzina, 2006); and $\hat{\boldsymbol{u}}^k(\boldsymbol{\xi}, \boldsymbol{x})$ and $\hat{\boldsymbol{t}}^k(\boldsymbol{\xi}, \boldsymbol{x})$ constitute the elastodynamic Green's function for a uniform semi-infinite solid by denoting the respective displacement and traction vectors at $\boldsymbol{\xi} \in \Omega$ due to a unit (time harmonic) point force acting at $\boldsymbol{x} \in \Omega$ in the kth direction.

For the ensuing treatment, the displacement field in (4) and (8) can be conveniently decomposed as

$$
\boldsymbol{u}(\boldsymbol{\xi}) = \boldsymbol{u}^{\mathrm{F}}(\boldsymbol{\xi}) + \tilde{\boldsymbol{u}}(\boldsymbol{\xi}), \quad \boldsymbol{\xi} \in \bar{\Omega}^-, \tag{10}
$$

where $\tilde{\boldsymbol{u}}$ denotes the scattered field, and

$$
\boldsymbol{u}^{\mathrm{F}}(\boldsymbol{x}) = \boldsymbol{e}_k \int_{V_f} \boldsymbol{f}(\boldsymbol{\xi}) \cdot \hat{\boldsymbol{u}}^k(\boldsymbol{\xi}, \boldsymbol{x}) \, \mathrm{d}\Omega_\xi \tag{11}
$$

is the free field defined as a response of the defect-free half-space Ω due to prescribed body force distribution $\boldsymbol{f}$. Under the implicit assumption that $\boldsymbol{u}^{\mathrm{F}}$ and $\tilde{\boldsymbol{u}}$ satisfy the radiation condition (9) individually, substitution of (10) into (8) leads to an integral representation of the scattered field

$$
\tilde{\boldsymbol{u}}(\boldsymbol{x}) = -\boldsymbol{e}_k \int_\Gamma \boldsymbol{u}(\boldsymbol{\xi}) \cdot \hat{\boldsymbol{t}}^k(\boldsymbol{\xi}, \boldsymbol{x}) \, \mathrm{d}\Gamma_\xi + \boldsymbol{e}_k \int_\Gamma \boldsymbol{t}(\boldsymbol{\xi}) \cdot \hat{\boldsymbol{u}}^k(\boldsymbol{\xi}, \boldsymbol{x}) \, \mathrm{d}\Gamma_\xi, \quad \boldsymbol{x} \in \Omega^- \tag{12}
$$

that will be instrumental for the ensuing developments. By virtue of (10) and the integral identity in terms of $\boldsymbol{u}^{\mathrm{F}}$ (see Pak and Guzina, 1999), formula (12) can also be rewritten as

$$
\tilde{\boldsymbol{u}}(\boldsymbol{x}) = -\boldsymbol{e}_k \int_\Gamma \tilde{\boldsymbol{u}}(\boldsymbol{\xi}) \cdot \hat{\boldsymbol{t}}^k(\boldsymbol{\xi}, \boldsymbol{x}) \, \mathrm{d}\Gamma_\xi + \boldsymbol{e}_k \int_\Gamma \tilde{\boldsymbol{t}}(\boldsymbol{\xi}) \cdot \hat{\boldsymbol{u}}^k(\boldsymbol{\xi}, \boldsymbol{x}) \, \mathrm{d}\Gamma_\xi, \quad \boldsymbol{x} \in \Omega^-, \tag{13}
$$

featuring the boundary values of $\tilde{\boldsymbol{u}}$ and $\tilde{\boldsymbol{t}} = \boldsymbol{n} \cdot \boldsymbol{C} : \nabla\tilde{\boldsymbol{u}}$.

On the basis of (10), a *reference* value of the cost functional (1) can be introduced as

$$
\mathscr{J}(\Omega, \boldsymbol{m}; \boldsymbol{f}) \equiv \mathscr{J}(\Omega; \boldsymbol{f}) = \int_{\Pi^{\mathrm{obs}}} \varphi(\boldsymbol{u}^{\mathrm{F}}, \boldsymbol{u}^{\mathrm{obs}}) \, \mathrm{d}\Pi_\xi; \tag{14}
$$

a quantity that is calculated with reference to the *unperturbed* (i.e. obstacle-free) background domain Ω.

3. Topological sensitivity

To aid the gradient-based minimization of (1) that is often used as a tool for identifying Δ_{true} on the basis of motion measurements $\boldsymbol{u}^{\mathrm{obs}}$, of interest in this study is the development of

material-topological derivative for the class of cost functionals $\mathscr{J}(\Omega^-, \boldsymbol{m}; \boldsymbol{f})$ given by (1) that would provide a reliable preliminary information about the location, geometry and material characteristics of the hidden defect. In situations when $\mathscr{J}$ is a non-convex function in the material-geometric parametric space used to describe the defect (as is often the case), the quality of such preliminary information may be a critical factor in ensuring that the minimization scheme converges to the global minimum of $\mathscr{J}$ rather than its local counterpart.

To this end, let $\mathscr{B} \subset \mathbb{R}^3$ be a *fixed*, simply-connected open set of volume $|\mathscr{B}|$ containing the origin, and let $\mathscr{B}_a = \boldsymbol{x}^{\mathrm{o}} + a\mathscr{B} \subset \Omega$ denote the region of volume $|\mathscr{B}_a| \equiv a^3|\mathscr{B}|$ that is occupied by a small inclusion with size $a > 0$ (see Fig. 1) and material properties $\boldsymbol{m} = (\mu^\star, v^\star, \rho^\star)$. Further, let $\mathscr{B}_a$ have a smooth boundary $\mathscr{S}_a = \partial\mathscr{B}_a$ of class C^1. Generalizing upon the results in Guzina and Bonnet (2004), one is in particular interested in the asymptotic behavior of (1) with $\Delta \equiv \mathscr{B}_a$ as $a \to 0$. With reference to this limiting behavior, the topological derivative, $\mathscr{T}$, of $\mathscr{J}$ at $\boldsymbol{x}^{\mathrm{o}}$ can be introduced through the expansion

$$\mathscr{J}(\Omega \backslash \bar{\mathscr{B}}_a, \boldsymbol{m}; \boldsymbol{f}) = \mathscr{J}(\Omega; \boldsymbol{f}) + h(a)\mathscr{T}(\boldsymbol{x}^{\mathrm{o}}, \boldsymbol{m}; \boldsymbol{f}) + o(h(a)) \quad \text{as } a \to 0, \ \mathscr{B}_a(\boldsymbol{x}^{\mathrm{o}}) \subset \Omega,$$
(15)

where $\mathscr{J}(\Omega; \boldsymbol{f})$ is given by (14) and $h(a)$, identified with the leading term, is to be determined. In the sequel, it is assumed that

$$h(a) > 0, \ \lim_{a \to 0} h(a) = 0, \quad |\mathscr{T}(\boldsymbol{x}^{\mathrm{o}}, \boldsymbol{m}; \boldsymbol{f})| < \infty, \ \boldsymbol{x}^{\mathrm{o}} \in \Omega$$
(16)

as a prerequisite for topological sensitivity to make sense. If $\lim_{a \to 0} h(a) = 0$ as postulated in (16), one finds from (15) that

$$\mathscr{T}(\boldsymbol{x}^{\mathrm{o}}, \boldsymbol{m}; \boldsymbol{f}) = \lim_{a \to 0} \frac{\mathscr{J}(\Omega \backslash \bar{\mathscr{B}}_a, \boldsymbol{m}; \boldsymbol{f}) - \mathscr{J}(\Omega; \boldsymbol{f})}{h(a)}$$
(17)

which justifies the use of term "derivative" in the context of $\mathscr{T}$. One may note that this definition is not restricted to spherical obstacles for which $\mathscr{B}$ is the unit ball, $\partial\mathscr{B} = \mathscr{S}$ is the unit sphere, and $|\mathscr{B}| = 4\pi/3$. In the context of elastostatics and structural shape optimization (Eschenauer et al., 1994; Sokolowski and Zochowski, 1999), it was shown that the spatial distribution of $\mathscr{T}(\boldsymbol{x}^{\mathrm{o}}, \boldsymbol{0}; \boldsymbol{f})|_{\omega=0}$ can be used as a powerful criterion for the removal of spare material through regions where $\mathscr{T} < 0$. Similarly, elastodynamic results in Guzina and Bonnet (2004) and Bonnet and Guzina (2004) highlight the potential of $\mathscr{T}(\boldsymbol{x}^{\mathrm{o}}, \boldsymbol{0}; \boldsymbol{f})$ for preliminary identification of subsurface cavities through an assembly of sampling points, $\boldsymbol{x}^{\mathrm{o}}$, where the topological sensitivity attains pronounced *negative* values. A primary motivation for such methodologies revolves around the notion that points where $\mathscr{T} < 0$, and in particular those with marked negative values of $\mathscr{T}$, indicate locations where the removal of "excess" material (effected via cavity nucleation) is most effective as measured by the rate of decrease of $\mathscr{J}(\Omega)$ in (15). In view of their fundamental premise of a nucleating cavity (i.e. $\boldsymbol{m} = \boldsymbol{0}$), however, the existing methodologies and in particular those in Guzina and Bonnet (2004) and Bonnet and Guzina (2004) are not equipped to deal with obstacles of general nature; a limitation that this study aims to transcend.

To provide a further rationale for (15) and (16) in light of the *distinct* topologies characterizing Ω and $\Omega \backslash \bar{\mathscr{B}}_a$, it is useful to employ the implicit hypothesis that $\bar{\mathscr{B}}_a \cap \Pi^{\mathrm{obs}} = \emptyset$ and represent the perturbation (i.e. scattering) effect of $\mathscr{B}_a$ on $\mathscr{J}$ via a system of traction discontinuities acting across $\mathscr{S}_a = \partial\mathscr{B}_a$ in the unperturbed (i.e. obstacle-free) solid Ω.

Accordingly, one may write

$$\mathscr{J}(\Omega\backslash\bar{\mathscr{B}}_a, \boldsymbol{m}; \boldsymbol{f}) = \mathscr{J}(\Omega; \boldsymbol{f} + \boldsymbol{\tau}^a \delta_{\mathscr{S}_a}), \tag{18}$$

where $\boldsymbol{\tau}^a$ signifies a suitable jump in tractions across $\mathscr{S}_a$; $\delta_{\mathscr{S}_a}$ denotes the surface delta function over $\mathscr{S}_a$ (Vladimirov, 1979), and $\mathscr{J}(\Omega; \cdot)$ is given by (14). To understand the nature of $\boldsymbol{\tau}^a$, consider the solution of the transmission problem given by (4)–(7) and (9) when $\varDelta = \mathscr{B}_a$. Next, assume that the total displacement field $\boldsymbol{u}$ over $\varPi^{\mathrm{obs}} \subset \Omega^- \cup \Sigma$, used to compute the left-hand side of (18), permits a representation in terms of the single-layer potential

$$\boldsymbol{u}(\boldsymbol{x}) = \boldsymbol{u}^{\mathrm{F}}(\boldsymbol{x}) + \boldsymbol{e}_k \int_{\mathscr{S}_a} \boldsymbol{\varphi}(\boldsymbol{\xi}) \cdot \hat{\boldsymbol{u}}^k(\boldsymbol{\xi}, \boldsymbol{x}) \, \mathrm{d}\mathscr{S}_{\xi}, \quad \boldsymbol{x} \in \varPi^{\mathrm{obs}}, \tag{19}$$

over $\mathscr{S}_a$ where $\hat{\boldsymbol{u}}^k$ is the Green's function for the *unperturbed* reference solid Ω. By virtue of the jump relationships for the conormal derivative (in this case the traction on $\mathscr{S}_a$) in terms of a single-layer potential, see McLean (2000), one finds that in fact $\boldsymbol{\tau}^a = \boldsymbol{\varphi}$. As an alternative argument one may rewrite (19), using the surface delta function over $\mathscr{S}_a$, as a volume potential

$$\boldsymbol{u}(\boldsymbol{x}) = \boldsymbol{u}^{\mathrm{F}}(\boldsymbol{x}) + \boldsymbol{e}_k \int_{\Omega} \boldsymbol{\varphi}(\boldsymbol{\xi}) \cdot \hat{\boldsymbol{u}}^k(\boldsymbol{\xi}, \boldsymbol{x}) \, \delta_{\mathscr{S}_a}(\boldsymbol{\xi}) \, \mathrm{d}\Omega_{\xi}, \quad \boldsymbol{x} \in \varPi^{\mathrm{obs}}. \tag{20}$$

On employing the definition of $\boldsymbol{u}^{\mathrm{F}}$ in (11) and the reciprocity of the half-space Green's function (Guzina et al., 2003) whereby $\hat{u}^k_j(\boldsymbol{\xi}, \boldsymbol{x}) = \hat{u}^j_k(\boldsymbol{x}, \boldsymbol{\xi})$, (20) can be expressed in the component notation as

$$\begin{aligned}
\boldsymbol{u}(\boldsymbol{x}) &= \boldsymbol{e}_k \left\{ u^{\mathrm{F}}_k + \int_{\Omega} \hat{u}^j_k(\boldsymbol{x}, \boldsymbol{\xi}) \varphi_j(\boldsymbol{\xi}) \delta_{\mathscr{S}_a}(\boldsymbol{\xi}) \, \mathrm{d}\Omega_{\xi} \right\} \\
&= \boldsymbol{e}_k \int_{\Omega} \hat{u}^j_k(\boldsymbol{x}, \boldsymbol{\xi}) \{ f_j + \varphi_j \delta_{\mathscr{S}_a} \}(\boldsymbol{\xi}) \, \mathrm{d}\Omega_{\xi}, \quad \boldsymbol{x} \in \varPi^{\mathrm{obs}},
\end{aligned} \tag{21}$$

from which it immediately follows that $\boldsymbol{\tau}^a = \boldsymbol{\varphi}$, cf. (18). In this setting, the small-defect expansion (15) can thus be re-interpreted as one with respect to the body-force excitation in lieu of domain topology. With reference to (17) and (18), hypothesis $|\mathscr{T}| < \infty$ will thus make sense if, for example, $\boldsymbol{\tau}^a$ remains bounded on $\mathscr{B}_a$ as $a \to 0$. For the problem of spherical cavity nucleation (Guzina and Bonnet, 2004), it can be shown that the latter condition holds (e.g. Kupradze, 1965) provided that $\bar{\mathscr{B}}_a$ is outside of the support ($V_{\mathrm{f}} \subset \Omega$) of the body force $\boldsymbol{f}$ generating $\boldsymbol{u}^{\mathrm{F}}$. In the sequel, it will likewise be assumed that $V_{\mathrm{f}} \cap \bar{\mathscr{B}}_a = \emptyset$ for the nucleating inclusion problem.

4. Asymptotic for a nucleating inclusion

To arrive at a compact expression for (17) when $\boldsymbol{m}$ is non-trivial, integral representation (12) when $\varGamma = \mathscr{S}_a$ and $\tilde{\boldsymbol{u}} = \tilde{\boldsymbol{u}}^a$ can be conveniently rewritten by virtue of (10) as

$$\begin{aligned}
\tilde{\boldsymbol{u}}^a(\boldsymbol{x}) &= -\boldsymbol{e}_k \int_{\mathscr{S}_a} \hat{\boldsymbol{t}}^k(\boldsymbol{\xi}, \boldsymbol{x}) \cdot \boldsymbol{u}^{\mathrm{F}}(\boldsymbol{\xi}) \, \mathrm{d}\mathscr{S}_{\xi} - \boldsymbol{e}_k \int_{\mathscr{S}_a} \hat{\boldsymbol{t}}^k(\boldsymbol{\xi}, \boldsymbol{x}) \cdot \tilde{\boldsymbol{u}}^a(\boldsymbol{\xi}) \, \mathrm{d}\mathscr{S}_{\xi} \\
&\quad + \boldsymbol{e}_k \int_{\mathscr{S}_a} \hat{\boldsymbol{u}}^k(\boldsymbol{\xi}, \boldsymbol{x}) \cdot \boldsymbol{t}^a(\boldsymbol{\xi}) \, \mathrm{d}\mathscr{S}_{\xi} \\
&\equiv \mathscr{I}^1(\boldsymbol{x}) + \mathscr{I}^2(\boldsymbol{x}) + \mathscr{I}^3(\boldsymbol{x}), \quad \boldsymbol{x} \in \Omega^- = \Omega\backslash\bar{\mathscr{B}}_a,
\end{aligned} \tag{22}$$

where $\boldsymbol{n}$ denotes the unit normal on $\mathscr{S}_a = \partial\mathscr{B}_a$ oriented toward the interior of $\mathscr{B}_a$; $\boldsymbol{t}^a = \boldsymbol{n} \cdot \boldsymbol{C} : \nabla(\boldsymbol{u}^{\mathrm{F}} + \tilde{\boldsymbol{u}}^a)$, and $\mathscr{I}^1$, $\mathscr{I}^2$, and $\mathscr{I}^3$ denote, respectively, the three integrals on the

right-hand side of (22). Note that the order of multiplicands in each *scalar* product has been reversed relative to those in (12) to facilitate the ensuing derivation. By means of the divergence theorem and Taylor expansion of the featured elastodynamic fields around $\xi = x^\circ$, the limiting behavior of the first and the third integral in (22) as $a \to 0$ can be, respectively, reduced to

$$\mathscr{I}^1(x) = a^3 |\mathscr{B}| e_k \{ \hat{\boldsymbol{\sigma}}^k(x^\circ, x) : \boldsymbol{D} : \boldsymbol{\sigma}^{\mathrm{F}}(x^\circ) - \rho \omega^2 \hat{\boldsymbol{u}}^k(x^\circ, x) \cdot \boldsymbol{u}^{\mathrm{F}}(x^\circ) \} + \mathrm{o}(a^3),$$
$$x \in \Omega^-, \quad a \to 0 \tag{23}$$

and

$$\mathscr{I}^3(x) = -a^3 |\mathscr{B}| e_k \{ \hat{\boldsymbol{\sigma}}^k(x^\circ, x) : \boldsymbol{D} : \overset{\star}{\boldsymbol{\sigma}}{}^a(x^\circ) - \rho^\star \omega^2 \hat{\boldsymbol{u}}^k(x^\circ, x) \cdot \overset{\star}{\boldsymbol{u}}{}^a(x^\circ) \} + \mathrm{o}(a^3),$$
$$x \in \Omega^-, \quad a \to 0, \tag{24}$$

where $\boldsymbol{\sigma}^{\mathrm{F}} = \boldsymbol{C} : \nabla \boldsymbol{u}^{\mathrm{F}}$ is the free-field stress tensor; $\overset{\star}{\boldsymbol{\sigma}}{}^a = \boldsymbol{C}^\star : \nabla \overset{\star}{\boldsymbol{u}}{}^a$ is the stress field inside the vanishing inclusion, and

$$\boldsymbol{D} = \frac{1}{3\kappa} \boldsymbol{E}_1 + \frac{1}{2\mu} \boldsymbol{E}_2 \tag{25}$$

is the elastic compliance tensor characterizing the semi-infinite solid Ω^-. With reference to (22)–(23), it is important to note that the limiting expression for $\mathscr{I}^1$ is fully explicit as it involves only the free field (known beforehand) and the elastodynamic Green's function. This is, however, not the case with $\mathscr{I}^2$ and $\mathscr{I}^3$ which entail a full solution to the forward scattering problem. The remainder of this section focuses on resolving the two latter fields.

4.1. Boundary variation of the scattered field

To elucidate the contribution of $\mathscr{I}^2$ in (22) for vanishing a, it is necessary first to determine the limiting behavior of the scattered field, $\tilde{\boldsymbol{u}}^a$, along $\mathscr{S}_a$ as $a \to 0$. In what follows, the notation "$\boldsymbol{v} = O(a^\kappa)$" where $\boldsymbol{v}$ is a vector field will be used in lieu of $v_i = O(a^\kappa)$, $i \in \{1, 2, 3\}$. In general, one may expect that the scattered field will vanish with diminishing obstacle size, whereas the free field is independent of a so that

$$\boldsymbol{u}^{\mathrm{F}}(\xi) = O(1), \quad \tilde{\boldsymbol{u}}^a(\xi) = o(1) \text{ as } a \to 0, \quad \xi \in \Omega^- \cup \mathscr{S}_a \cup \Sigma. \tag{26}$$

On the basis of (4)–(7) and (10), the field equations and boundary conditions for the solid obstacle problem in terms of the scattered field can be written as

$$\nabla \cdot (\boldsymbol{C} : \nabla \tilde{\boldsymbol{u}}^a) = -\rho \omega^2 \tilde{\boldsymbol{u}}^a, \quad \xi \in \Omega^-,$$
$$\tilde{\boldsymbol{t}}^a = 0, \quad \xi \in \Sigma,$$
$$\tilde{\boldsymbol{u}}^a + \boldsymbol{u}^{\mathrm{F}} = \overset{\star}{\boldsymbol{u}}{}^a, \quad \tilde{\boldsymbol{t}}^a + \boldsymbol{t}^{\mathrm{F}} = -\overset{\star}{\boldsymbol{t}}{}^a, \quad \xi \in \mathscr{S}_a,$$
$$\nabla \cdot (\boldsymbol{C}^\star : \nabla \overset{\star}{\boldsymbol{u}}{}^a) = -\rho^\star \omega^2 \overset{\star}{\boldsymbol{u}}{}^a, \quad \xi \in \mathscr{B}_a, \tag{27}$$

where $\tilde{\boldsymbol{t}}^a = \boldsymbol{n} \cdot \boldsymbol{C} : \nabla \tilde{\boldsymbol{u}}^a$; $\boldsymbol{t}^{\mathrm{F}} = \boldsymbol{n} \cdot \boldsymbol{C} : \nabla \boldsymbol{u}^{\mathrm{F}}$; $\overset{\star}{\boldsymbol{t}}{}^a = -\boldsymbol{n} \cdot \boldsymbol{C}^\star : \nabla \overset{\star}{\boldsymbol{u}}{}^a$, and $\tilde{\boldsymbol{u}}^a$ satisfies the generalized radiation condition (9) as examined earlier. As shown in Pak and Guzina (1999), (27) is governed by a pair of regularized (i.e. Cauchy principal value-free) boundary integral

equations, the first of which refers to the exterior domain Ω^- and can be written as

$$\boldsymbol{e}_k \cdot \tilde{\boldsymbol{u}}^a(\boldsymbol{x}) + \int_{\mathscr{S}_a} (\tilde{\boldsymbol{u}}^a(\boldsymbol{\xi}) - \tilde{\boldsymbol{u}}^a(\boldsymbol{x})) \cdot [\hat{\boldsymbol{t}}^k(\boldsymbol{\xi}, \boldsymbol{x})]_1 \, \mathrm{d}\mathscr{S}_{\xi} + \int_{\mathscr{S}_a} \tilde{\boldsymbol{u}}^a(\boldsymbol{\xi}) \cdot [\hat{\boldsymbol{t}}^k(\boldsymbol{\xi}, \boldsymbol{x})]_2 \, \mathrm{d}\mathscr{S}_{\xi}$$

$$- \int_{\mathscr{S}_a} \tilde{\boldsymbol{t}}^a(\boldsymbol{\xi}) \cdot \hat{\boldsymbol{u}}^k(\boldsymbol{\xi}, \boldsymbol{x}) \, \mathrm{d}\mathscr{S}_{\xi} = 0, \quad \boldsymbol{x} \in \mathscr{S}_a, \ k \in \{1, 2, 3\}, \tag{28}$$

where $\hat{\boldsymbol{t}} = \boldsymbol{n} \cdot \boldsymbol{C} : \nabla\hat{\boldsymbol{u}}$. Similarly the second equation, written for the inclusion, reads

$$\int_{\mathscr{S}_a} (\overset{\star}{\boldsymbol{u}}^a(\boldsymbol{\xi}) - \overset{\star}{\boldsymbol{u}}^a(\boldsymbol{x})) \cdot [\check{\boldsymbol{t}}^k(\boldsymbol{\xi}, \boldsymbol{x})]_1 \, \mathrm{d}\mathscr{S}_{\xi} + \int_{\mathscr{S}_a} \overset{\star}{\boldsymbol{u}}^a(\boldsymbol{\xi}) \cdot [\check{\boldsymbol{t}}^k(\boldsymbol{\xi}, \boldsymbol{x})]_2 \, \mathrm{d}\mathscr{S}_{\xi}$$

$$- \int_{\mathscr{S}_a} \overset{\star}{\boldsymbol{t}}^a(\boldsymbol{\xi}) \cdot \check{\boldsymbol{u}}^k(\boldsymbol{\xi}, \boldsymbol{x}) \, \mathrm{d}\mathscr{S}_{\xi} = 0, \quad \boldsymbol{x} \in \mathscr{S}_a, \ k \in \{1, 2, 3\}, \tag{29}$$

where $\check{\boldsymbol{u}}^k$ and $\check{\boldsymbol{t}}^k = -\boldsymbol{n} \cdot \boldsymbol{C}^{\star} : \nabla\check{\boldsymbol{u}}^k$ refer to the elastodynamic fundamental solution for an infinite solid $\mathbb{R}^3$ with elastic parameters $\mu^{\star}$ and $v^{\star}$, and mass density $\rho^{\star}$. Recalling (27), the two integral equations are linked through the interfacial conditions

$$\tilde{\boldsymbol{u}}^a(\boldsymbol{\xi}) + \boldsymbol{u}^{\mathrm{F}}(\boldsymbol{\xi}) = \overset{\star}{\boldsymbol{u}}^a(\boldsymbol{\xi}), \quad \tilde{\boldsymbol{t}}^a(\boldsymbol{\xi}) + \boldsymbol{t}^{\mathrm{F}}(\boldsymbol{\xi}) = -\overset{\star}{\boldsymbol{t}}^a(\boldsymbol{\xi}), \ \boldsymbol{\xi} \in \mathscr{S}_a, \tag{30}$$

which are repeated for further reference. As examined in Pak and Guzina (1999), $\tilde{\boldsymbol{u}}^a$ and $\overset{\star}{\boldsymbol{u}}^a$ are required to be Hölder-continuous on $\mathscr{S}_a$ with continuity index $0 < \gamma \leqslant 1$; a condition that is stronger than (standard) continuity, but weaker than differentiability if $\gamma < 1$ (Kellogg, 1954). In the context of this study, it is noted that the afore made assumption $\boldsymbol{u} \in C^2(\Omega^-) \cap C^1(\bar{\Omega}^-)$, which implies $\boldsymbol{u} \in C^1(\mathscr{S}_a)$, ensures that $\boldsymbol{u}$ are Hölder-continuous with $\gamma = 1$. With such hypothesis, (28) and (29) are regularized using a decomposition of the respective Green's functions (Guzina and Pak, 2001) into their singular part $[\cdot]_1$ and a residual, i.e. regular part $[\cdot]_2$ according to

$$\hat{\boldsymbol{u}}^k = [\hat{\boldsymbol{u}}^k]_1 + [\hat{\boldsymbol{u}}^k]_2, \quad \hat{\boldsymbol{t}}^k = [\hat{\boldsymbol{t}}^k]_1 + [\hat{\boldsymbol{t}}^k]_2,$$
$$\check{\boldsymbol{u}}^k = [\check{\boldsymbol{u}}^k]_1 + [\check{\boldsymbol{u}}^k]_2, \quad \check{\boldsymbol{t}}^k = [\check{\boldsymbol{t}}^k]_1 + [\check{\boldsymbol{t}}^k]_2. \tag{31}$$

Here $[\check{\boldsymbol{u}}]_1$ and $[\check{\boldsymbol{t}}]_1$ are given by the (elastostatic) Kelvin's solution for an infinite solid with elastic constants $\mu^{\star}$ and $v^{\star}$, while, for point forces located at a non-zero distance from the free surface (i.e. $\boldsymbol{x} \cdot \boldsymbol{e}_3 > 0$), $[\hat{\boldsymbol{u}}]_1$ and $[\hat{\boldsymbol{t}}]_1$ coincide with the Kelvin's solution with elastic parameters μ and v (Pak and Guzina, 1999). With reference to (28) as an example, the regularization is performed by (i) employing the integral representation of the scattered field (13) in terms of $\tilde{\boldsymbol{u}}^a$, (ii) adding the regularizing term $\boldsymbol{e}_k \int_{\mathscr{S}_a} \tilde{\boldsymbol{u}}^a(\boldsymbol{x}) \cdot [\hat{\boldsymbol{t}}^k(\boldsymbol{\xi}, \boldsymbol{x})]_1 \, \mathrm{d}\mathscr{S}_{\xi}$ to both sides of the equation, (iii) taking the limit as $\boldsymbol{x} \to \Gamma = \mathscr{S}_a$, and (iv) using the fact that $\lim_{\boldsymbol{x} \to \mathscr{S}_a} \int_{\mathscr{S}_a} [\hat{\boldsymbol{t}}^k(\boldsymbol{\xi}, \boldsymbol{x})]_1 \, \mathrm{d}\mathscr{S}_{\xi} = 0$ when $\boldsymbol{x} \in \Omega^-$ by virtue of static equilibrium. The derivation of (29) follows along similar lines, using the regularizing term $\boldsymbol{e}_k \int_{\mathscr{S}_a} \overset{\star}{\boldsymbol{u}}^a(\boldsymbol{x}) \cdot [\check{\boldsymbol{t}}^k(\boldsymbol{\xi}, \boldsymbol{x})]_1 \, \mathrm{d}\mathscr{S}_{\xi}$, $\boldsymbol{x} \in \mathscr{B}_a$ and the fact that $\lim_{\boldsymbol{x} \to \mathscr{S}_a} \int_{\mathscr{S}_a} [\check{\boldsymbol{t}}^k(\boldsymbol{\xi}, \boldsymbol{x})]_1 \, \mathrm{d}\mathscr{S}_{\xi} = -\boldsymbol{e}_k$ when $\boldsymbol{x} \in \mathscr{B}_a$ which results in the cancellation of the "free" term, $\overset{\star}{\boldsymbol{u}}^a(\boldsymbol{x})$.

Owing to the singular nature of the elastostatic fundamental solution (Bonnet, 1999) constituting $[\cdot]_1$ and the intrinsic regularity of residual components $[\cdot]_2$, one has

$$[\hat{\boldsymbol{u}}^k(\boldsymbol{\xi}, \boldsymbol{x})]_1 = O(\varepsilon^{-1}), \quad [\hat{\boldsymbol{u}}^k(\boldsymbol{\xi}, \boldsymbol{x})]_2 = O(1),$$
$$[\hat{\boldsymbol{t}}^k(\boldsymbol{\xi}, \boldsymbol{x})]_1 = O(\varepsilon^{-2}), \quad [\hat{\boldsymbol{t}}^k(\boldsymbol{\xi}, \boldsymbol{x})]_2 = O(1),$$

$$[\check{\boldsymbol{u}}^k(\boldsymbol{\xi},\boldsymbol{x})]_1 = O(\varepsilon^{-1}), \quad [\check{\boldsymbol{u}}^k(\boldsymbol{\xi},\boldsymbol{x})]_2 = O(1) \text{ as } \varepsilon = |\boldsymbol{\xi}-\boldsymbol{x}| \to 0,$$

$$[\check{\boldsymbol{t}}^k(\boldsymbol{\xi},\boldsymbol{x})]_1 = O(\varepsilon^{-2}), \quad [\check{\boldsymbol{t}}^k(\boldsymbol{\xi},\boldsymbol{x})]_2 = O(1). \tag{32}$$

For the ensuing discussion, it is useful to employ (31) further and expand (28) as

$$\tilde{\boldsymbol{u}}^a(\boldsymbol{x}) \cdot \left\{ \boldsymbol{e}_k + \underline{\int_{\mathscr{S}_a} [\hat{\boldsymbol{t}}^k(\boldsymbol{\xi},\boldsymbol{x})]_2 \, \mathrm{d}\mathscr{S}_\xi} \right\} + \int_{\mathscr{S}_a} (\tilde{\boldsymbol{u}}^a(\boldsymbol{\xi}) - \tilde{\boldsymbol{u}}^a(\boldsymbol{x})) \cdot \{[\hat{\boldsymbol{t}}^k(\boldsymbol{\xi},\boldsymbol{x})]_1 + \underline{\hat{\boldsymbol{t}}^k(\boldsymbol{\xi},\boldsymbol{x})]_2}\} \, \mathrm{d}\mathscr{S}_\xi$$

$$- \int_{\mathscr{S}_a} \tilde{\boldsymbol{t}}^a(\boldsymbol{\xi}) \cdot \{[\hat{\boldsymbol{u}}^k(\boldsymbol{\xi},\boldsymbol{x})]_1 + \underline{[\hat{\boldsymbol{u}}^k(\boldsymbol{\xi},\boldsymbol{x})]_2}\} \, \mathrm{d}\mathscr{S}_\xi = 0, \quad \boldsymbol{x} \in \mathscr{S}_a. \tag{33}$$

By virtue of (32) and the fact that $\mathscr{S}_a = O(a^2)$, it immediately follows that the underlined terms in (33) are of *higher order* than their braced companions as $a \to 0$. Applying a similar procedure to (29), one finds that

$$\underline{\overset{\star}{\boldsymbol{u}}{}^a(\boldsymbol{x}) \cdot \int_{\mathscr{S}_a} [\check{\boldsymbol{t}}^k(\boldsymbol{\xi},\boldsymbol{x})]_2 \, \mathrm{d}\mathscr{S}_\xi} + \int_{\mathscr{S}_a} (\overset{\star}{\boldsymbol{u}}{}^a(\boldsymbol{\xi}) - \overset{\star}{\boldsymbol{u}}{}^a(\boldsymbol{x})) \cdot \{[\check{\boldsymbol{t}}^k(\boldsymbol{\xi},\boldsymbol{x})]_1 + \underline{\check{\boldsymbol{t}}^k(\boldsymbol{\xi},\boldsymbol{x})]_2}\} \, \mathrm{d}\mathscr{S}_\xi$$

$$- \int_{\mathscr{S}_a} \overset{\star}{\boldsymbol{t}}{}^a(\boldsymbol{\xi}) \cdot \{[\check{\boldsymbol{u}}^k(\boldsymbol{\xi},\boldsymbol{x})]_1 + \underline{[\check{\boldsymbol{u}}^k(\boldsymbol{\xi},\boldsymbol{x})]_2}\} \, \mathrm{d}\mathscr{S}_\xi = 0, \quad \boldsymbol{x} \in \mathscr{S}_a. \tag{34}$$

Here again the last two underlined terms are of higher order than their braced companions as $a \to 0$ due to (32). To justify the smallness of the first term in (34) for vanishing a, on the other hand, it is useful to recall (26) which implies that $\overset{\star}{\boldsymbol{u}}{}^a = \boldsymbol{u}^{\mathrm{F}} + \tilde{\boldsymbol{u}}^a = O(1)$ on $\mathscr{S}_a$ as $a \to 0$. On the basis of this result, the relationship $\mathscr{S}_a = O(a^2)$ and (32), the claim is established by the fact that

$$\overset{\star}{\boldsymbol{u}}{}^a(\boldsymbol{x}) \cdot \int_{\mathscr{S}_a} [\check{\boldsymbol{t}}^k(\boldsymbol{\xi},\boldsymbol{x})]_2 \, \mathrm{d}\mathscr{S}_\xi = O(a^2),$$

$$\int_{\mathscr{S}_a} (\overset{\star}{\boldsymbol{u}}{}^a(\boldsymbol{\xi}) - \overset{\star}{\boldsymbol{u}}{}^a(\boldsymbol{x})) \cdot [\check{\boldsymbol{t}}^k(\boldsymbol{\xi},\boldsymbol{x})]_1 \, \mathrm{d}\mathscr{S}_\xi = O(a^\gamma) \quad \text{as } a \to 0,$$

where $0 < \gamma \leqslant 1$ is the Hölder index characterizing the continuity of $\overset{\star}{\boldsymbol{u}}{}^a$ on $\mathscr{S}_a$.

To fully expose the limiting behavior of (33) and (34) as $a \to 0$, one may introduce the scaled coordinates

$$\boldsymbol{\xi} = a\boldsymbol{\zeta} + \boldsymbol{x}^{\mathrm{o}}, \quad \boldsymbol{x} = a\boldsymbol{y} + \boldsymbol{x}^{\mathrm{o}}, \tag{35}$$

and formally denote the leading asymptotic behaviors of the featured elastodynamic fields on $\mathscr{S}_a$ as

$$\underset{a \to 0}{\mathrm{Asym}} \, \tilde{\boldsymbol{u}}^a(\boldsymbol{\xi}) \equiv a\,\tilde{\boldsymbol{\vartheta}}(\boldsymbol{\zeta}), \quad \underset{a \to 0}{\mathrm{Asym}} \, \tilde{\boldsymbol{t}}^a(\boldsymbol{\xi}) \equiv \tilde{\boldsymbol{\tau}}(\boldsymbol{\zeta}),$$

$$\underset{a \to 0}{\mathrm{Asym}} \, \overset{\star}{\boldsymbol{u}}{}^a(\boldsymbol{\xi}) \equiv \boldsymbol{u}^{\mathrm{F}}(\boldsymbol{x}^{\mathrm{o}}) + a\,\overset{\star}{\boldsymbol{\vartheta}}(\boldsymbol{\zeta}), \quad \underset{a \to 0}{\mathrm{Asym}} \, \overset{\star}{\boldsymbol{t}}{}^a(\boldsymbol{\xi}) \equiv \boldsymbol{\tau}^\star(\boldsymbol{\zeta}), \quad \boldsymbol{\xi} \in \mathscr{S}_a, \ \boldsymbol{\zeta} \in \mathscr{S}, \tag{36}$$

where $\mathscr{S} = \partial\mathscr{B}$ is the "unit" surface ($\mathscr{S}_a|_{a=1}$) as examined in Section 3. On combining the interfacial conditions (30) with Taylor expansion of free field at $\boldsymbol{x} = \boldsymbol{x}^{\mathrm{o}}$, namely

$$\boldsymbol{u}^{\mathrm{F}}(\boldsymbol{\xi}) = \boldsymbol{u}^{\mathrm{F}}(\boldsymbol{x}^{\mathrm{o}}) + (\boldsymbol{\xi} - \boldsymbol{x}^{\mathrm{o}}) \cdot \nabla\boldsymbol{u}^{\mathrm{F}}(\boldsymbol{x}^{\mathrm{o}}) + O(a^2),$$

$$\boldsymbol{t}^{\mathrm{F}}(\boldsymbol{\xi}) = \boldsymbol{n}(\boldsymbol{\xi}) \cdot \boldsymbol{\sigma}^{\mathrm{F}}(\boldsymbol{x}^{\mathrm{o}}) + O(a), \quad \boldsymbol{\xi} \in \mathscr{S}_a, \ a \to 0, \tag{37}$$

it follows that the limiting quantities in (36) are related through

$$\tilde{\boldsymbol{\vartheta}}(\zeta) + \boldsymbol{\zeta} \cdot \nabla \boldsymbol{u}^{\mathrm{F}}(\boldsymbol{x}^{\mathrm{o}}) = \overset{\star}{\tilde{\boldsymbol{\vartheta}}}(\zeta), \quad \tilde{\boldsymbol{\tau}}(\zeta) + \boldsymbol{\eta}(\zeta) \cdot \boldsymbol{\sigma}^{\mathrm{F}}(\boldsymbol{x}^{\mathrm{o}}) = -\boldsymbol{\tau}^{\star}(\zeta), \quad \zeta \in \mathscr{S}, \tag{38}$$

where $\boldsymbol{\eta}(\zeta) = \boldsymbol{n}(\xi)$. With reference to (35) it can also be shown, using the explicit formulas for the Kelvin's solution (e.g. Pak and Guzina, 1999), that

$$[\hat{\boldsymbol{u}}^k(\xi, \boldsymbol{x})]_1 = \frac{1}{a}[\hat{\boldsymbol{u}}^k(\zeta, \boldsymbol{y})]_1, \quad [\hat{\boldsymbol{t}}^k(\xi, \boldsymbol{x})]_1 = \frac{1}{a^2}[\hat{\boldsymbol{t}}^k(\zeta, \boldsymbol{y})]_1,$$

$$[\breve{\boldsymbol{u}}^k(\xi, \boldsymbol{x})]_1 = \frac{1}{a}[\breve{\boldsymbol{u}}^k(\zeta, \boldsymbol{y})]_1, \quad [\breve{\boldsymbol{t}}^k(\xi, \boldsymbol{x})]_1 = \frac{1}{a^2}[\breve{\boldsymbol{t}}^k(\zeta, \boldsymbol{y})]_1, \quad a \to 0. \tag{39}$$

By virtue of (36) and (39) and the relationship

$$\mathrm{d}\mathscr{S}_\xi = a^2 \,\mathrm{d}\mathscr{S}_\zeta, \quad \xi \in \mathscr{S}_a, \ \zeta \in \mathscr{S},$$

the limiting form of (33) and (34) as $a \to 0$ can be synthesized, on dropping the (underlined) higher-order terms, in terms of the pair of normalized integral equations

$$\boldsymbol{e}_k \cdot \tilde{\boldsymbol{\vartheta}}(\boldsymbol{y}) + \int_{\mathscr{S}} (\tilde{\boldsymbol{\vartheta}}(\zeta) - \tilde{\boldsymbol{\vartheta}}(\boldsymbol{y})) \cdot [\hat{\boldsymbol{t}}^k(\zeta, \boldsymbol{y})]_1 \,\mathrm{d}\mathscr{S}_\zeta - \int_{\mathscr{S}} \tilde{\boldsymbol{\tau}}(\zeta) \cdot [\hat{\boldsymbol{u}}^k(\zeta, \boldsymbol{y})]_1 \,\mathrm{d}\mathscr{S}_\zeta = 0,$$

$$\int_{\mathscr{S}} (\overset{\star}{\tilde{\boldsymbol{\vartheta}}}(\zeta) - \overset{\star}{\tilde{\boldsymbol{\vartheta}}}(\boldsymbol{y})) \cdot [\breve{\boldsymbol{t}}^k(\zeta, \boldsymbol{y})]_1 \,\mathrm{d}\mathscr{S}_\zeta - \int_{\mathscr{S}} \boldsymbol{\tau}^{\star}(\zeta) \cdot [\breve{\boldsymbol{u}}^k(\zeta, \boldsymbol{y})]_1 \,\mathrm{d}\mathscr{S}_\zeta = 0, \quad \boldsymbol{y} \in \mathscr{S}, \tag{40}$$

where $k \in \{1, 2, 3\}$ and $[\cdot]_1$ are given by the Kelvin's solution in $\mathbb{R}^3$ as examined before. Here it is useful to note that (40) are independent of the defect size, a, so that $\tilde{\boldsymbol{\vartheta}} = O(1)$ as $a \to 0$. In view of this result and (36), it further follows that $\tilde{\boldsymbol{u}}^a(\xi) = O(a)$ as $a \to 0$ when $\xi \in \mathscr{S}_a$.

On inspection (cf. (28)–(30)), the system of integral equations given by (38) and (40) turns out to be associated with an *elastostatic* counterpart of the dynamic transmission problem (27). In particular, one finds that

$$\nabla_\zeta \cdot (\boldsymbol{C} : \nabla_\zeta \tilde{\boldsymbol{\vartheta}}) = \boldsymbol{0}, \quad \zeta \in \mathbb{R}^3 \backslash \bar{\mathscr{B}},$$

$$\tilde{\boldsymbol{\vartheta}} + \boldsymbol{\zeta} \cdot \nabla \boldsymbol{u}^{\mathrm{F}}(\boldsymbol{x}^{\mathrm{o}}) = \overset{\star}{\tilde{\boldsymbol{\vartheta}}}, \quad \zeta \in \mathscr{S},$$

$$\tilde{\boldsymbol{\tau}} + \boldsymbol{\eta} \cdot \boldsymbol{\sigma}^{\mathrm{F}}(\boldsymbol{x}^{\mathrm{o}}) = -\boldsymbol{\tau}^{\star}, \quad \zeta \in \mathscr{S},$$

$$\nabla_\zeta \cdot (\boldsymbol{C}^{\star} : \nabla_\zeta \overset{\star}{\tilde{\boldsymbol{\vartheta}}}) = \boldsymbol{0}, \quad \zeta \in \mathscr{B} \tag{41}$$

in an *infinite* solid, where $\tilde{\boldsymbol{\tau}} = \boldsymbol{\eta} \cdot \boldsymbol{C} : \nabla_\zeta \tilde{\boldsymbol{\vartheta}}$ in $\mathbb{R}^3 \backslash \bar{\mathscr{B}}$; $\boldsymbol{\tau}^{\star} = -\boldsymbol{\eta} \cdot \boldsymbol{C}^{\star} : \nabla_\zeta \overset{\star}{\tilde{\boldsymbol{\vartheta}}}$ in $\mathscr{B}$, and, precluding rigid-body rotation,

$$\nabla \boldsymbol{u}^{\mathrm{F}}(\boldsymbol{x}^{\mathrm{o}}) = \boldsymbol{D} : \boldsymbol{\sigma}^{\mathrm{F}}(\boldsymbol{x}^{\mathrm{o}}), \tag{42}$$

with $\boldsymbol{D}$ given by (25). To ensure the uniqueness of the solution, (41) are augmented by the regularity condition (replacing (9)) which requires that $\tilde{\boldsymbol{\vartheta}}(\zeta) = O(|\zeta|^{-1})$ as $\zeta \to \infty$. In this way (41) describe the response, in terms of the perturbation displacement field $\tilde{\boldsymbol{\vartheta}}$ in $\mathbb{R}^3 \backslash \bar{\mathscr{B}}$, of an elastic full-space (containing an inclusion) that is subjected to a *constant* state of stress, $\boldsymbol{\sigma}^{\mathrm{F}}(\boldsymbol{x}^{\mathrm{o}})$, at infinity. To aid the ensuing developments, the solution of (41) can be conveniently decomposed as

$$\tilde{\boldsymbol{\vartheta}}(\zeta) = \sigma_{kl}^{\mathrm{F}}(\boldsymbol{x}^{\mathrm{o}}) \tilde{\boldsymbol{\vartheta}}^{kl}(\zeta), \quad \zeta \in \mathscr{S}, \ k, l \in \{1, 2, 3\}, \tag{43}$$

where $\tilde{\boldsymbol{\vartheta}}^{kl} = \tilde{\boldsymbol{\vartheta}}^{lk} = O(1)$, that are *independent* of both x^{o} and a, solve (41) and (42) with $\boldsymbol{\sigma}^{\mathrm{F}}(x^{\mathrm{o}}) = \frac{1}{2}(\boldsymbol{e}_k \otimes \boldsymbol{e}_l + \boldsymbol{e}_l \otimes \boldsymbol{e}_k)$. On the basis of (36)–(43), the contribution of the last term in (22) for the vanishing obstacle size can be written as

$$\mathscr{I}^2(\boldsymbol{x}) = -a^3|\mathscr{B}|\,\boldsymbol{e}_k\{\hat{\boldsymbol{\sigma}}^k(x^{\mathrm{o}},\boldsymbol{x}) : \mathscr{V}(\boldsymbol{m}) : \boldsymbol{\sigma}^{\mathrm{F}}(x^{\mathrm{o}})\} + o(a^3), \quad \boldsymbol{x} \in \Omega^-, \ a \to 0,$$

$$\mathscr{V}(\boldsymbol{m}) = \frac{1}{|\mathscr{B}|}\left\{\int_{\partial\mathscr{B}} \tilde{\vartheta}_i^{kl}(\boldsymbol{\zeta})\,\eta_j(\boldsymbol{\zeta})\,\mathrm{d}\mathscr{S}_{\zeta}\right\}\boldsymbol{e}_i \otimes \boldsymbol{e}_j \otimes \boldsymbol{e}_k \otimes \boldsymbol{e}_l. \tag{44}$$

4.2. Elastodynamic field in the interior of a vanishing obstacle

With reference to (24), an explicit characterization of the third integral in (22) in the limit as $a \to 0$ requires the knowledge of the displacement and stress fields inside the obstacle for vanishing a. To this end, it is useful to recall (36) which yields

$$\overset{\star}{\boldsymbol{u}}^a(\boldsymbol{\xi}) = \boldsymbol{u}^{\mathrm{F}}(x^{\mathrm{o}}) + a\,\overset{\star}{\boldsymbol{\vartheta}}(\boldsymbol{\zeta}) + o(a), \quad \boldsymbol{\xi} \in \mathscr{S}_a, \ \boldsymbol{\zeta} \in \mathscr{S}, \ a \to 0, \tag{45}$$

where $\boldsymbol{\zeta} = (\boldsymbol{\xi} - x^{\mathrm{o}})/a$ as examined earlier. Since both $\overset{\star}{\boldsymbol{u}}^a(\boldsymbol{\xi})$ and $\overset{\star}{\boldsymbol{\vartheta}}(\boldsymbol{\zeta}(\boldsymbol{\xi}))$ are analytic for $\boldsymbol{\xi} \in \mathscr{B}_a$, the above equality must also hold inside the obstacle so that

$$\overset{\star}{\boldsymbol{u}}^a(\boldsymbol{\xi}) = \boldsymbol{u}^{\mathrm{F}}(x^{\mathrm{o}}) + o(1),$$

$$\nabla\overset{\star}{\boldsymbol{u}}^a(\boldsymbol{\xi}) = \nabla_{\zeta}\overset{\star}{\boldsymbol{\vartheta}}(\boldsymbol{\zeta}) + o(1), \quad \boldsymbol{\xi} \in \mathscr{B}_a, \ a \to 0. \tag{46}$$

By virtue of (41) and (42), it can also be seen that $\overset{\star}{\boldsymbol{\vartheta}}(\boldsymbol{\zeta})$ is linear in $\boldsymbol{\sigma}^{\mathrm{F}}(x^{\mathrm{o}})$ and consequently

$$\overset{\star}{\boldsymbol{\sigma}}^a(x^{\mathrm{o}}) = \boldsymbol{C}^{\star} : \nabla\overset{\star}{\boldsymbol{u}}^a(x^{\mathrm{o}}) = \boldsymbol{C}^{\star} : \nabla_{\zeta}\overset{\star}{\boldsymbol{\vartheta}}(\boldsymbol{0}) + o(1) \equiv \mathscr{Q}(\boldsymbol{m}) : \boldsymbol{\sigma}^{\mathrm{F}}(x^{\mathrm{o}}) + o(1), \quad a \to 0, \tag{47}$$

where $\mathscr{Q}_{ijkl} = \mathscr{Q}_{jikl} = \mathscr{Q}_{ijlk}$ $(i,j,k,l \in \{1,2,3\})$ in general depend on the shape and material properties $(\boldsymbol{m})$ of the inclusion, but are independent of x^{o} and a. On the basis of (46) and (47), integral (24) can now be rewritten more explicitly as

$$\mathscr{I}^3(\boldsymbol{x}) = -a^3|\mathscr{B}|\boldsymbol{e}_k\{\hat{\boldsymbol{\sigma}}^k(x^{\mathrm{o}},\boldsymbol{x}) : [\boldsymbol{D} : \mathscr{Q}(\boldsymbol{m})] : \boldsymbol{\sigma}^{\mathrm{F}}(x^{\mathrm{o}})$$
$$- \rho^{\star}\omega^2\hat{\boldsymbol{u}}^k(x^{\mathrm{o}},\boldsymbol{x}) \cdot \boldsymbol{u}^{\mathrm{F}}(x^{\mathrm{o}})\} + o(a^3), \quad \boldsymbol{x} \in \Omega^-, \ a \to 0, \tag{48}$$

where $\boldsymbol{D}$ is the compliance tensor given in (25).

On summing (23), (44) and (48) according to (22), the limiting behavior of the scattered field for a vanishing inclusion of arbitrary shape can be written as

$$\tilde{\boldsymbol{u}}^a(\boldsymbol{x}) = a^3|\mathscr{B}|\,\boldsymbol{e}_k\{\hat{\boldsymbol{\sigma}}^k(x^{\mathrm{o}},\boldsymbol{x}) : [\boldsymbol{D} : (\boldsymbol{I}_4 - \mathscr{Q}(\boldsymbol{m})) - \mathscr{V}(\boldsymbol{m})] : \boldsymbol{\sigma}^{\mathrm{F}}(x^{\mathrm{o}})$$
$$- (\rho - \rho^{\star})\omega^2\,\hat{\boldsymbol{u}}^k(x^{\mathrm{o}},\boldsymbol{x}) \cdot \boldsymbol{u}^{\mathrm{F}}(x^{\mathrm{o}})\} + o(a^3), \quad \boldsymbol{x} \in \Omega^-, \ a \to 0, \tag{49}$$

where $\boldsymbol{D}$, $\mathscr{V}$ and $\mathscr{Q}$ are (for a given $\mathscr{B}$ and $\boldsymbol{m}$) constant fourth-order tensors defined, respectively, in (25), (44) and (47). One may note that the values of $\tilde{\boldsymbol{u}}^a(\boldsymbol{x})$ for $\boldsymbol{x} \in \Omega^-$ behave as $O(a^3)$ when $a \to 0$, whereas their boundary counterparts on $\mathscr{S}_a$ behave as $O(a)$ as examined earlier. Given the fact that both $\boldsymbol{x} \in \Omega^-$ and $x^{\mathrm{o}} \in \mathscr{B}_a$ are fixed during the limiting process whereby $(\boldsymbol{\xi} - \boldsymbol{x})|_{\mathscr{S}_a} = O(|x^{\mathrm{o}} - \boldsymbol{x}|) = O(1)$ with vanishing a, this relationship can be best understood by considering the second integral on the right-hand side of (22) as an example and noting that $\tilde{\boldsymbol{u}}^a|_{\mathscr{S}_a} = O(a)$, $\mathscr{S}_a = O(a^2)$, and $\hat{\boldsymbol{t}}^k(\boldsymbol{\xi},\boldsymbol{x})|_{\mathscr{S}_a} = O(1)$ as $a \to 0$.

5. Sensitivity formulas

5.1. Direct formulation

By virtue of (10) and (49), one may expand (1) with respect to the scattered field caused by the vanishing obstacle, $\tilde{\boldsymbol{u}}^a = \boldsymbol{u}^a - \boldsymbol{u}^F$, as

$$\mathcal{J}(\Omega \backslash \bar{\mathscr{B}}_a, \boldsymbol{m}; \boldsymbol{f}) = \mathcal{J}(\Omega; \boldsymbol{f}) + \int_{\Pi^{\mathrm{obs}}} \mathrm{Re}\left\{\frac{\partial \varphi}{\partial \boldsymbol{u}}(\boldsymbol{u}^F, \boldsymbol{u}^{\mathrm{obs}}) \cdot \tilde{\boldsymbol{u}}^a\right\} \mathrm{d}\Pi_\xi + o(\|\tilde{\boldsymbol{u}}^a\|) \quad \text{as } a \to 0,$$

(50)

where

$$\frac{\partial \varphi}{\partial \boldsymbol{w}} \equiv \frac{\partial \varphi}{\partial \boldsymbol{w}_R} - i\frac{\partial \varphi}{\partial \boldsymbol{w}_I}, \quad \boldsymbol{w}_R = \mathrm{Re}(\boldsymbol{w}), \quad \boldsymbol{w}_I = \mathrm{Im}(\boldsymbol{w}).$$

(51)

Since $\partial \varphi / \partial \boldsymbol{u}(\boldsymbol{u}^F, \boldsymbol{u}^{\mathrm{obs}})$ is by definition independent of a, one finds from (15), (49) and (50) that $h(a) \propto a^3$ for the 3D nucleating inclusion problem; a behavior that conforms with the hypothesis $\lim_{a\to 0} h(a) = 0$ made in (16). Although the choice of multiplicative constant in the definition of $h(a)$ is by no means unique, it is assumed in this study that

$$h(a) = a^3 |\mathscr{B}|,$$

(52)

so that $h(a) > 0$ also holds. In general, however, the expression for $h(a)$ is expected to depend on both dimensionality of the problem and boundary conditions assumed over $\mathscr{S}_a$ (see, e.g., Garreau et al., 2001 in the context of Laplace problems and impenetrable obstacles). In contrast, $h(a)$ is independent of φ since $\partial \varphi / \partial \boldsymbol{u}(\boldsymbol{u}^F, \boldsymbol{u}^{\mathrm{obs}})$ in (50) does not vary with a.

From (15) and (50), one finds

$$\mathcal{T}(\boldsymbol{x}^\mathrm{o}, \boldsymbol{m}; \boldsymbol{f}) = \lim_{a\to 0} \frac{1}{h(a)} \int_{\Pi^{\mathrm{obs}}} \mathrm{Re}\left\{\frac{\partial \varphi}{\partial \boldsymbol{u}}(\boldsymbol{u}^F, \boldsymbol{u}^{\mathrm{obs}}) \cdot \tilde{\boldsymbol{u}}^a\right\} \mathrm{d}\Pi_\xi.$$

(53)

With (49), (52) and (53) the generalized formula for topological sensitivity, that postulates the nucleation of an infinitesimal *inclusion* ($\boldsymbol{m} \neq \boldsymbol{0}$) in an otherwise intact semi-infinite solid Ω, takes the explicit form

$$\mathcal{T}(\boldsymbol{x}^\mathrm{o}, \boldsymbol{m}; \boldsymbol{f}) = \int_{\Pi^{\mathrm{obs}}} \mathrm{Re}\left\{\frac{\partial \varphi}{\partial \boldsymbol{u}}(\boldsymbol{u}^F(\boldsymbol{\xi}), \boldsymbol{u}^{\mathrm{obs}}) \cdot e_k[\hat{\boldsymbol{\sigma}}^k(\boldsymbol{x}^\mathrm{o}, \boldsymbol{\xi}) : \mathscr{A}(\boldsymbol{m}) : \boldsymbol{\sigma}^F(\boldsymbol{x}^\mathrm{o})\right.$$
$$\left. -(\rho - \rho^\star)\omega^2 \hat{\boldsymbol{u}}^k(\boldsymbol{x}^\mathrm{o}, \boldsymbol{\xi}) \cdot \boldsymbol{u}^F(\boldsymbol{x}^\mathrm{o})]\right\} \mathrm{d}\Pi_\xi,$$

(54)

where

$$\mathscr{A}(\boldsymbol{m}) = \boldsymbol{D} : (\boldsymbol{I}_4 - \mathcal{Q}(\boldsymbol{m})) - \mathscr{V}(\boldsymbol{m}),$$

(55)

for an arbitrary (reference) shape $\mathscr{B}$. Here it is noted that the last hypothesis in (16), namely $|\mathcal{T}| < \infty$, implicitly holds as long as $\boldsymbol{x}^\mathrm{o} \notin \bar{V}_\mathrm{f}$ where V_f denotes the support of $\boldsymbol{f}$.

With reference to (1) and (54), an extension of the foregoing developments to multiple source distributions $\boldsymbol{f}^q$ ($q = 1, 2, \ldots, Q$), applied in sequence as a means to better "illuminate" subsurface defects, is straightforward and involves an external summation in the form

$$\mathcal{J}_f(\cdot, \cdot) \equiv \sum_{q=1}^{Q} \mathcal{J}(\cdot, \cdot; \boldsymbol{f}^q), \quad \mathcal{T}_f(\cdot, \cdot) \equiv \sum_{q=1}^{Q} \mathcal{T}(\cdot, \cdot; \boldsymbol{f}^q).$$

(56)

5.1.1. Nucleating ellipsoidal defect

For an arbitrary reference shape $\mathscr{B}$, the featured set of canonical problems given by (41) when $\boldsymbol{\sigma}^{\mathrm{F}}(\boldsymbol{x}^{\mathrm{o}}) = \frac{1}{2}(\boldsymbol{e}_k \otimes \boldsymbol{e}_l + \boldsymbol{e}_l \otimes \boldsymbol{e}_k)$, $k, l \in \{1, 2, 3\}$ can be solved numerically. In situations when $\mathscr{B}$ is an ellipsoid, on the other hand, (41) can be solved in closed form via the equivalent-eigenstrain method as in Mura (1987). By employing the latter approach (see Appendix A), it is in particular shown in (A.14) that the fourth-order tensor $\mathscr{V}$ takes an explicit form in terms of the Eshelby tensor, $\mathscr{S}$, as

$$\mathscr{V}(\boldsymbol{m}) = -\mathscr{S} : \mathscr{R}, \tag{57}$$

where

$$\mathscr{R} = ((\boldsymbol{C} - \boldsymbol{C}^\star) : \mathscr{S} - \boldsymbol{C})^{-1} : (\boldsymbol{C}^\star - \boldsymbol{C}) : \boldsymbol{D}. \tag{58}$$

Likewise, (A.11) demonstrates that the fourth-order tensor $\mathscr{Q}$ is such that

$$\boldsymbol{D} : \mathscr{Q}(\boldsymbol{m}) = \boldsymbol{D} : \boldsymbol{C}^\star : (\mathscr{S} : \mathscr{R} + \boldsymbol{D}), \tag{59}$$

when $\mathscr{B}$ is an ellipsoid. By virtue of (55) and (57)–(59), one finds as shown in (A.15) that $\mathscr{A} = \mathscr{R}$, i.e.

$$\mathscr{A}(\boldsymbol{m}) = ((\boldsymbol{C} - \boldsymbol{C}^\star) : \mathscr{S} - \boldsymbol{C})^{-1} : (\boldsymbol{C}^\star - \boldsymbol{C}) : \boldsymbol{D} \quad \text{(ELLIPSOID)}. \tag{60}$$

5.1.2. Nucleating spherical defect

When $\mathscr{B}$ is a unit ball, formula (60) can further be specialized by invoking the known expression for $\mathscr{S}$ dealing with the inclusions of spherical shape (Mura, 1987). In this way, $\mathscr{A}$ can be written in terms of its spherical and deviatoric components as

$$\mathscr{A}(\boldsymbol{m}) = \mathscr{R}_{\mathrm{sph}} \boldsymbol{E}_1 + \mathscr{R}_{\mathrm{dev}} \boldsymbol{E}_2 \quad \text{(BALL)}, \tag{61}$$

where $\boldsymbol{E}_1 = \frac{1}{3} \boldsymbol{I}_2 \otimes \boldsymbol{I}_2$ and $\boldsymbol{E}_2 = \boldsymbol{I}_4 - \boldsymbol{E}_1$ as examined earlier, and

$$\mathscr{R}_{\mathrm{sph}} = -\frac{1}{3\kappa} \frac{3(1-v)(\bar{\kappa}^\star - 1)}{(1+v)(\bar{\kappa}^\star - 1) + 3(1-v)}, \quad \bar{\kappa}^\star = \frac{\kappa^\star}{\kappa},$$

$$\mathscr{R}_{\mathrm{dev}} = -\frac{1}{2\mu} \frac{15(1-v)(\bar{\mu}^\star - 1)}{(8 - 10v)(\bar{\mu}^\star - 1) + 15(1-v)}, \quad \bar{\mu}^\star = \frac{\mu^\star}{\mu}. \tag{62}$$

On setting the material parameters of the inclusion to zero (i.e. $\boldsymbol{m} = \boldsymbol{0}$), formulas (61) and (62) can be shown to be in agreement with the results obtained in Guzina and Bonnet (2004) for the case of a nucleating spherical cavity. Moreover, when $\mu^\star = \mu$, $v^\star = v$ and $\rho^\star = \rho$ which corresponds to the case of a defect-free half-space, the right-hand side of (54) vanishes identically by virtue of either (60) or (61) and (62).

5.2. Adjoint field formulation

Formally, applicability of the foregoing developments is limited to "simple" reference domains (e.g. semi-infinite and infinite bodies with constant or functionally-graded elastic properties) for which the elastodynamic Green's function is available. To deal with the restriction, it is instructive to recast (54) within the framework of the adjoint field method that is often used in shape optimization analyses (e.g. Garreau et al., 2001; Samet et al., 2003).

As an illustration of the latter approach to topological sensitivity, attention is henceforth focused on *finite*, homogeneous reference bodies of arbitrary geometry. To this end,

consider a counterpart of the defect identification problem in Section 2 when Ω^- is finite and subjected to the *homogeneous* boundary conditions over its "external" boundary $\Sigma = \partial \Omega$, Ω being the (defect-free) reference domain. On denoting the Dirichlet and Neumann portions of Σ, respectively, by Σ_D and Σ_N (see Fig. 2) so that $\Sigma = \Sigma_D \cup \Sigma_N$, one finds with reference to (4)–(7) that

$$\nabla \cdot (\boldsymbol{C} : \nabla \boldsymbol{u}) + \boldsymbol{f} = -\rho \omega^2 \boldsymbol{u}, \quad \boldsymbol{\xi} \in \Omega^-,$$
$$\boldsymbol{u}(\boldsymbol{\xi}) = \boldsymbol{0}, \quad \boldsymbol{\xi} \in \Sigma_D,$$
$$\boldsymbol{t}(\boldsymbol{\xi}) = \boldsymbol{0}, \quad \boldsymbol{\xi} \in \Sigma_N,$$
$$\boldsymbol{u} = \overset{\star}{\boldsymbol{u}}, \quad \boldsymbol{t} = -\overset{\star}{\boldsymbol{t}}, \quad \boldsymbol{\xi} \in \Gamma,$$
$$\nabla \cdot (\boldsymbol{C}^\star : \nabla \overset{\star}{\boldsymbol{u}}) = -\rho^\star \omega^2 \overset{\star}{\boldsymbol{u}}, \quad \boldsymbol{\xi} \in \Delta. \tag{63}$$

As before, it is assumed that the defect is illuminated by a body-force excitation $\boldsymbol{f}$ with the induced motion ($\boldsymbol{u}^{\mathrm{obs}}$) monitored over a measurement surface $\Pi^{\mathrm{obs}} = \Pi_\Sigma^{\mathrm{obs}} \cup \Pi_\Omega^{\mathrm{obs}}$, where $\Pi_\Sigma^{\mathrm{obs}} = \Pi^{\mathrm{obs}} \cap \Sigma_N$ and $\Pi_\Omega^{\mathrm{obs}} = \Pi^{\mathrm{obs}} \cap \Omega$ denote, respectively, its boundary and interior segments (see Fig. 2).

In this setting, it is convenient to make use of the shape-sensitivity treatments of inverse scattering problems (Bonnet, 1995; Guzina et al., 2003) and introduce the so-called *adjoint field*, $\overset{\bullet}{\boldsymbol{u}}$, as an elastodynamic response of the defect-free body Ω due to virtual excitation

$$g(\boldsymbol{\xi}) = \frac{\partial \varphi}{\partial \boldsymbol{u}}(\boldsymbol{u}^{\mathrm{F}}(\boldsymbol{\xi}), \boldsymbol{u}^{\mathrm{obs}}), \quad \boldsymbol{\xi} \in \Pi^{\mathrm{obs}} \tag{64}$$

applied over the measurement surface so that its magnitude equals the misfit (in the sense of φ) between the experimental observations $\boldsymbol{u}^{\mathrm{obs}}$ and their free-field estimates $\boldsymbol{u}^{\mathrm{F}}$ where

$$\nabla \cdot (\boldsymbol{C} : \nabla \boldsymbol{u}^{\mathrm{F}}) + \boldsymbol{f} = -\rho \omega^2 \boldsymbol{u}^{\mathrm{F}}, \quad \boldsymbol{\xi} \in \Omega,$$
$$\boldsymbol{u}^{\mathrm{F}} = \boldsymbol{0}, \quad \boldsymbol{\xi} \in \Sigma_D,$$
$$\boldsymbol{t}^{\mathrm{F}} = \boldsymbol{0}, \quad \boldsymbol{\xi} \in \Sigma_N. \tag{65}$$
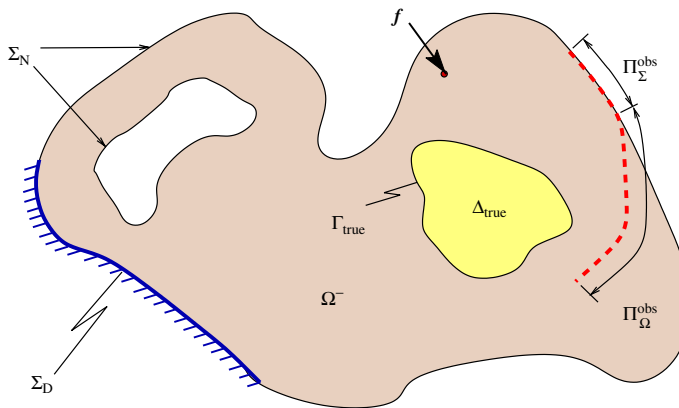

Fig. 2. Finite reference body.

Here again φ is a (smooth) measure of distance between its arguments that is used to construct the cost functional (1). From such hypotheses, it immediately follows that adjoint field satisfies the field equations and boundary conditions

$$\nabla \cdot (\boldsymbol{C} : \nabla \dot{\boldsymbol{u}}) + \boldsymbol{g}\delta_{\Pi_\Omega^{\mathrm{obs}}} = -\rho\omega^2 \dot{\boldsymbol{u}}, \quad \boldsymbol{\xi} \in \Omega,$$

$$\dot{\boldsymbol{u}} = \boldsymbol{0}, \quad \boldsymbol{\xi} \in \Sigma_{\mathrm{D}},$$

$$\dot{\boldsymbol{t}} = \boldsymbol{0}, \quad \boldsymbol{\xi} \in \Sigma_{\mathrm{N}} \backslash \Pi_\Sigma^{\mathrm{obs}},$$

$$\dot{\boldsymbol{t}} = \boldsymbol{g}, \quad \boldsymbol{\xi} \in \Pi_\Sigma^{\mathrm{obs}}, \tag{66}$$

where $\dot{\boldsymbol{t}} = \boldsymbol{n} \cdot \boldsymbol{C} : \nabla \dot{\boldsymbol{u}}$; $\delta_{\Pi_\Omega^{\mathrm{obs}}}$ is the surface delta function over the interior segment of the measurement surface, and the body-force density $\boldsymbol{g}\delta_{\Pi_\Omega^{\mathrm{obs}}}$ is to be interpreted in the sense of a single-layer potential over $\Pi_\Omega^{\mathrm{obs}}$ (Vladimirov, 1979).

To obtain an adjoint-field counterpart of the shape sensitivity formula (54), it is next necessary to establish the finite-body equals of equations (27) governing the scattered field $\tilde{\boldsymbol{u}}^a$ caused by the presence of an infinitesimal flaw $\mathscr{B}_a$ in an otherwise defect-free body Ω. Indeed, from (63) and (65) one finds by setting $\Delta = \mathscr{B}_a$ and $\Gamma = \mathscr{S}_a$ that

$$\nabla \cdot (\boldsymbol{C} : \nabla \tilde{\boldsymbol{u}}^a) = -\rho\omega^2 \tilde{\boldsymbol{u}}^a, \quad \boldsymbol{\xi} \in \Omega \backslash \bar{\mathscr{B}}_a,$$

$$\tilde{\boldsymbol{u}}^a = \boldsymbol{0}, \quad \boldsymbol{\xi} \in \Sigma_{\mathrm{D}},$$

$$\tilde{\boldsymbol{t}}^a = \boldsymbol{0}, \quad \boldsymbol{\xi} \in \Sigma_{\mathrm{N}},$$

$$\tilde{\boldsymbol{u}}^a + \boldsymbol{u}^{\mathrm{F}} = \overset{\star}{\boldsymbol{u}}{}^a, \quad \tilde{\boldsymbol{t}}^a + \boldsymbol{t}^{\mathrm{F}} = -\overset{\star}{\boldsymbol{t}}{}^a, \; \boldsymbol{\xi} \in \mathscr{S}_a,$$

$$\nabla \cdot (\boldsymbol{C}^\star : \nabla \overset{\star}{\boldsymbol{u}}{}^a) = -\rho^\star\omega^2 \overset{\star}{\boldsymbol{u}}{}^a, \quad \boldsymbol{\xi} \in \mathscr{B}_a. \tag{67}$$

An application of the Graffi's reciprocity identity (Achenbach, 2003) to elastodynamic fields $\dot{\boldsymbol{u}}$ and $\tilde{\boldsymbol{u}}^a$ over the "punctured" body $\Omega \backslash \bar{\mathscr{B}}_a$ with boundary $\Sigma \cup \mathscr{S}_a$ can be formally written as

$$\int_{\Sigma \cup \mathscr{S}_a} \{\tilde{\boldsymbol{t}}^a \cdot \dot{\boldsymbol{u}} - \dot{\boldsymbol{t}} \cdot \tilde{\boldsymbol{u}}^a\} \, \mathrm{d}\mathscr{S}_\xi = \int_{\Omega \backslash \bar{\mathscr{B}}_a} \{\dot{\boldsymbol{f}} \cdot \tilde{\boldsymbol{u}}^a - \tilde{\boldsymbol{f}}^a \cdot \dot{\boldsymbol{u}}\} \, \mathrm{d}\Omega_\xi,$$

where $\dot{\boldsymbol{f}}$ and $\tilde{\boldsymbol{f}}^a$ are the body-force distributions associated, respectively, with $\dot{\boldsymbol{u}}$ and $\tilde{\boldsymbol{u}}^a$. With reference to (66) and (67), one finds that $\dot{\boldsymbol{f}} = \boldsymbol{g}\delta_{\Pi_\Omega^{\mathrm{obs}}}, \tilde{\boldsymbol{f}}^a = \boldsymbol{0}$, and further

$$\int_{\mathscr{S}_a} \{\tilde{\boldsymbol{t}}^a \cdot \dot{\boldsymbol{u}} - \dot{\boldsymbol{t}} \cdot \tilde{\boldsymbol{u}}^a\} \, \mathrm{d}\mathscr{S}_\xi = \int_{\Omega \backslash \bar{\mathscr{B}}_a} \boldsymbol{g}\delta_{\Pi_\Omega^{\mathrm{obs}}} \cdot \tilde{\boldsymbol{u}}^a \, \mathrm{d}\Omega_\xi + \int_{\Pi_\Sigma^{\mathrm{obs}}} \boldsymbol{g} \cdot \tilde{\boldsymbol{u}}^a \, \mathrm{d}\Pi_\xi$$

$$= \int_{\Pi^{\mathrm{obs}}} \frac{\partial\varphi}{\partial\boldsymbol{u}}(\boldsymbol{u}^{\mathrm{F}}, \boldsymbol{u}^{\mathrm{obs}}) \cdot \tilde{\boldsymbol{u}}^a \, \mathrm{d}\Pi_\xi, \tag{68}$$

which makes use of (64) and the fact that $\dot{\boldsymbol{u}} = \tilde{\boldsymbol{u}}^a = \boldsymbol{0}$ on Σ_{D}, $\tilde{\boldsymbol{t}}^a = \boldsymbol{0}$ on Σ_{N} and $\dot{\boldsymbol{t}} = \boldsymbol{g}$ on $\Pi_\Sigma^{\mathrm{obs}} \subseteq \Sigma_{\mathrm{N}}$. By virtue of (53) and (68), it immediately follows that

$$\mathscr{T}(\boldsymbol{x}^\circ, \boldsymbol{m}; \boldsymbol{f}) = \lim_{a \to 0} \frac{1}{h(a)} \mathrm{Re}\left\{\int_{\mathscr{S}_a} \left\{\dot{\boldsymbol{u}} \cdot \tilde{\boldsymbol{t}}^a - \tilde{\boldsymbol{u}}^a \cdot \dot{\boldsymbol{t}}\right\} \mathrm{d}\mathscr{S}_\xi\right\}, \tag{69}$$

where the order of multiplicands in each scalar product is reversed relative to those in (68) for convenience of derivation. On the basis of an asymptotic analysis similar to that highlighted in Section 4.1, it can be shown that for any fixed $\boldsymbol{x}^\circ \in \Omega$, the variation of $\tilde{\boldsymbol{u}}^a$ on $\mathscr{S}_a$ as $a \to 0$ is again given by the first equation in (36) where $\tilde{\boldsymbol{\vartheta}}$ solves the elastostatic

transmission problem (41) in $\mathbb{R}^3$. By virtue of this result and decomposition (43), one finds that

$$\tilde{\boldsymbol{u}}^a(\boldsymbol{\xi}) = a\sigma_{kl}^{\mathrm{F}}(\boldsymbol{x}^\circ)\tilde{\boldsymbol{\vartheta}}^{kl}(\boldsymbol{\zeta}) + o(a) \quad \text{as } a \to 0, \quad \boldsymbol{\xi} \in \mathscr{S}_a, \ \boldsymbol{\zeta} \in \mathscr{S}, \tag{70}$$

where the scaled coordinate $\boldsymbol{\zeta}$ is defined by (35) and $\tilde{\boldsymbol{\vartheta}}^{kl}$ ($k, l \in \{1, 2, 3\}$) solve (41) when $\boldsymbol{\sigma}^{\mathrm{F}}(\boldsymbol{x}^\circ) = \frac{1}{2}(\boldsymbol{e}_k \otimes \boldsymbol{e}_l + \boldsymbol{e}_l \otimes \boldsymbol{e}_k)$. From (70), the symmetry of $\overset{\bullet}{\boldsymbol{\sigma}}$, and Taylor expansion of the adjoint-field traction at $\boldsymbol{x}^\circ$, namely

$$\overset{\bullet}{\boldsymbol{u}}(\boldsymbol{\xi}) = \overset{\bullet}{\boldsymbol{u}}(\boldsymbol{x}^\circ) + (\boldsymbol{\xi} - \boldsymbol{x}^\circ) \cdot \nabla \overset{\bullet}{\boldsymbol{u}}(\boldsymbol{x}^\circ) + O(a^2)$$

$$\Longrightarrow \overset{\bullet}{\boldsymbol{t}}(\boldsymbol{\xi}) = \boldsymbol{n}(\boldsymbol{\xi}) \cdot \overset{\bullet}{\boldsymbol{\sigma}}(\boldsymbol{x}^\circ) + O(a), \quad \boldsymbol{\xi} \in \mathscr{S}_a, \ a \to 0, \tag{71}$$

it follows that

$$\int_{\mathscr{S}_a} \tilde{\boldsymbol{u}}^a \cdot \overset{\bullet}{\boldsymbol{t}} \, \mathrm{d}\mathscr{S}_{\xi} = a^3 \, \overset{\bullet}{\sigma}_{ij}(\boldsymbol{x}^\circ) \, \sigma_{kl}^{\mathrm{F}}(\boldsymbol{x}^\circ) \int_{\mathscr{S}} \vartheta_i^{kl}(\boldsymbol{\zeta}) \eta_j(\boldsymbol{\zeta}) \, \mathrm{d}\mathscr{S}_{\zeta} + o(a^3)$$

$$= a^3 |\mathscr{B}| \{ \overset{\bullet}{\boldsymbol{\sigma}}(\boldsymbol{x}^\circ) : \mathscr{V}(\boldsymbol{m}) : \boldsymbol{\sigma}^{\mathrm{F}}(\boldsymbol{x}^\circ) \} + o(a^3) \quad \text{as } a \to 0, \tag{72}$$

where $\mathscr{V}(\boldsymbol{m})$ is the fourth-order tensor defined in (44). On employing the divergence theorem and following the limiting analysis as in (45)–(47), it can also be shown that

$$\int_{\mathscr{S}_a} \overset{\bullet}{\boldsymbol{u}} \cdot \tilde{\boldsymbol{t}}^a \, \mathrm{d}\mathscr{S}_{\xi} = \int_{\mathscr{S}_a} \overset{\bullet}{\boldsymbol{u}} \cdot \boldsymbol{t}^a \, \mathrm{d}\mathscr{S}_{\xi} - \int_{\mathscr{S}_a} \overset{\bullet}{\boldsymbol{u}} \cdot \boldsymbol{t}^{\mathrm{F}} \, \mathrm{d}\mathscr{S}_{\xi}$$

$$= -\int_{\mathscr{B}_a} \nabla \cdot (\overset{\bullet}{\boldsymbol{u}} \cdot \overset{\star}{\boldsymbol{\sigma}}{}^a) \, \mathrm{d}\mathscr{B}_{\xi} + \int_{\mathscr{B}_a} \nabla \cdot (\overset{\bullet}{\boldsymbol{u}} \cdot \boldsymbol{\sigma}^{\mathrm{F}}) \, \mathrm{d}\mathscr{B}_{\xi}$$

$$= a^3 |\mathscr{B}| \{ \overset{\bullet}{\boldsymbol{\sigma}}(\boldsymbol{x}^\circ) : [\boldsymbol{D} : (\boldsymbol{I}_4 - \mathscr{Q}(\boldsymbol{m}))] : \boldsymbol{\sigma}^{\mathrm{F}}(\boldsymbol{x}^\circ) - (\rho - \rho^\star)\omega^2 \boldsymbol{u}^{\mathrm{F}}(\boldsymbol{x}^\circ) \cdot \overset{\bullet}{\boldsymbol{u}}(\boldsymbol{x}^\circ) \}$$

$$+ o(a^3) \quad \text{as } a \to 0, \tag{73}$$

where $\mathscr{Q}(\boldsymbol{m})$ is defined via (47). Note that (73) makes use of the symmetries of $\overset{\star}{\boldsymbol{\sigma}}{}^a = \boldsymbol{C}^\star : \nabla \overset{\star}{\boldsymbol{u}}{}^a$ and $\boldsymbol{\sigma}^{\mathrm{F}} = \boldsymbol{C} : \nabla \boldsymbol{u}^{\mathrm{F}}$, where $\overset{\star}{\boldsymbol{u}}{}^a$ is the elastodynamic displacement inside the obstacle featured in (67).

On the basis of (69), (72) and (73), the adjoint-field expression for generalized topological sensitivity takes the form

$$\mathscr{T}(\boldsymbol{x}^\circ, \boldsymbol{m}; \boldsymbol{f}) = \mathrm{Re}\{\overset{\bullet}{\boldsymbol{\sigma}}(\boldsymbol{x}^\circ) : \mathscr{A}(\boldsymbol{m}) : \boldsymbol{\sigma}^{\mathrm{F}}(\boldsymbol{x}^\circ) - (\rho - \rho^\star)\omega^2 \overset{\bullet}{\boldsymbol{u}}(\boldsymbol{x}^\circ) \cdot \boldsymbol{u}^{\mathrm{F}}(\boldsymbol{x}^\circ)\},$$

$$\mathscr{A}(\boldsymbol{m}) = \boldsymbol{D} : (\boldsymbol{I}_4 - \mathscr{Q}(\boldsymbol{m})) - \mathscr{V}(\boldsymbol{m}), \tag{74}$$

in terms of the elastodynamic fields $\boldsymbol{u}^{\mathrm{F}}$ and $\overset{\bullet}{\boldsymbol{u}}$, both computed for the *defect-free* reference body Ω. As in (54), explicit expressions for $\mathscr{A}(\boldsymbol{m})$ are again given by (60) and (61) in situations where the nucleating inclusion is ellipsoidal and spherical, respectively. One may observe that formula (74), although obtained using the boundary integral approach, is amenable to evaluation via *any* viable computational scheme, e.g. finite difference, finite element, or boundary element method.

To examine the relationship between the adjoint-field formulation and its "direct" counterpart, it is useful to consider the Green's function $\hat{\boldsymbol{u}}^k(\boldsymbol{\xi}, \boldsymbol{x})$ for the finite reference body Ω as an elastodynamic state that satisfies (65) with $\boldsymbol{f}(\boldsymbol{\xi}) = \delta(\boldsymbol{\xi} - \boldsymbol{x})\boldsymbol{e}_k$. Under the aforementioned hypotheses that Ω is uniform and subject to homogeneous (Dirichlet and/ or Neumann) boundary conditions, it can be shown as in Achenbach (2003) that $\hat{\boldsymbol{u}}^k$ is reciprocal, i.e. that $\hat{u}_i^k(\boldsymbol{\xi}, \boldsymbol{x}) = \hat{u}_k^i(\boldsymbol{x}, \boldsymbol{\xi})$. By virtue of the latter identity, (64) and (66), the

Somigliana-type integral representation of the adjoint field can be written as

$$\overset{\bullet}{\boldsymbol{u}}(\boldsymbol{x}^{\mathrm{o}}) = \int_{\Pi^{\mathrm{obs}}} \left\{ \frac{\partial \varphi}{\partial \boldsymbol{u}} (\boldsymbol{u}^{\mathrm{F}}(\boldsymbol{\xi}), \boldsymbol{u}^{\mathrm{obs}}) \cdot \boldsymbol{e}_k \right\} \hat{\boldsymbol{u}}^k(\boldsymbol{x}^{\mathrm{o}}, \boldsymbol{\xi}) \, \mathrm{d}\Pi_{\xi}. \quad \boldsymbol{x}^{\mathrm{o}} \in \Omega \tag{75}$$

which demonstrates that the sensitivity formulas (54) and (74) are in fact equivalent. In this sense the so-called direct formulation, elucidated in Section 5.1, applies equally to more complex (e.g. finite) reference domains Ω as long as (i) the single-layer potential (75) is evaluated *numerically* as an elastodynamic state solving (66), and (ii) decomposition (31) of the Green's function for the reference domain Ω (into a Kelvin-singular and a regular part) *applies* regardless of the fact that $\hat{\boldsymbol{u}}$ is not available explicitly.

6. Results and discussion

As shown in Guzina and Bonnet (2004) and Bonnet and Guzina (2004), the nucleating-cavity analogues of (54) and (74) can be used as a robust tool for the preliminary 3D reconstruction of impenetrable defects in the context of inverse scattering. Owing to their explicit dependence on the material properties of a nucleating inclusion, on the other hand, (54) and (74) carry an additional potential for *material identification* trough a parametric variation of $\boldsymbol{m}$ geared toward minimizing the value of $\mathcal{T}(\boldsymbol{x}^{\mathrm{o}}, \boldsymbol{m}; \boldsymbol{f})$ at a selected (i.e. fixed) sampling point $\boldsymbol{x}^{\mathrm{o}}$. To cater for applications such as material characterization medical diagnosis, the latter possibility is investigated next through a set of numerical examples. In what follows, the results are based on the direct-approach formula (54) and a ball-shaped nucleating defect unless stated otherwise.

Consider the synthetic testing configuration in Fig. 3 involving a semi-infinite reference solid with the shear modulus μ, Poisson's ratio $v = 0.3$ and mass density ρ. In sequence, the obstacle (or a system thereof) is illuminated by $Q = 16$ time-harmonic, "vertical" point sources uniformly spaced over a square surface grid of dimensions $18d \times 18d$. For each source location $\boldsymbol{x}^q$ ($q = 1, 2, \ldots, Q$), the induced surface motion is monitored over $M = 11 \times 11 = 121$ control points $\boldsymbol{x}^m \in \Sigma$ ($m = 1, 2, \ldots, M$), regularly distributed over a square
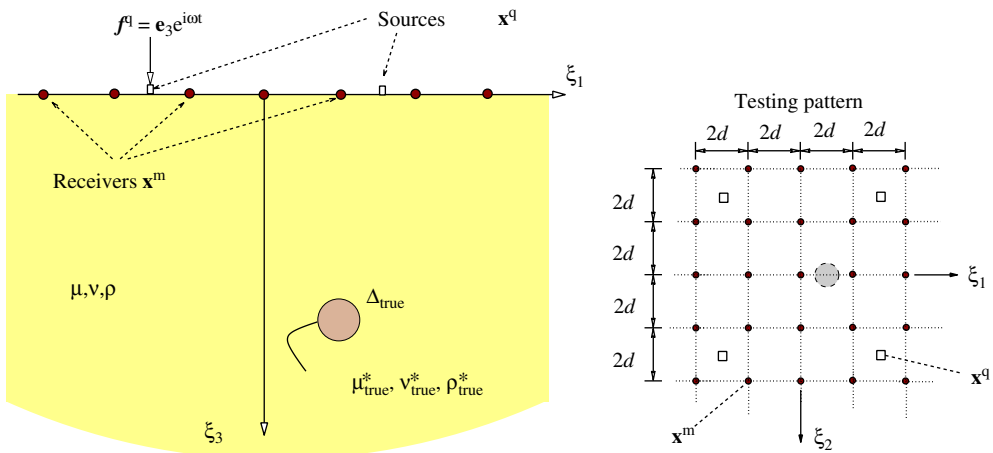
Fig. 3. Synthetic testing configuration.

grid of dimensions $20d \times 20d$. For this class of problems, it is convenient to supersede $\mathscr{J}$ and $\mathscr{T}$ by their multiple-source generalizations in (56) and to specify the distance function φ in (1) and (54) to a discrete least-squares format by taking

$$\varphi(\boldsymbol{u}, \boldsymbol{u}^{\mathrm{obs}}) = \tfrac{1}{2} \overline{(\boldsymbol{u} - \boldsymbol{u}^{\mathrm{obs}})} \cdot \boldsymbol{W} \cdot (\boldsymbol{u} - \boldsymbol{u}^{\mathrm{obs}}),$$

$$\boldsymbol{W} = \boldsymbol{W}(\boldsymbol{\xi}) = \sum_{m=1}^{M} W_{ij}^m \delta(\boldsymbol{\xi} - \boldsymbol{x}^m) \boldsymbol{e}_i \otimes \boldsymbol{e}_j, \quad i,j \in \{1,2,3\}, \tag{76}$$

where δ stands for the three-dimensional Dirac delta function; $\boldsymbol{e}_j$ is the unit vector in the ξ_j-direction; over-bar symbol denotes complex conjugation, and W_{ij}^m are suitable constants chosen so that they form Hermitian and positive-definite weighting matrices $\boldsymbol{W}^m$, $m = 1, 2, \ldots, M$.

6.1. Single defect

In the first set of examples, the center of a "true" spherical defect, of diameter $D = 0.8d$, is located at $(d, 0, 3d)$ (see also Fig. 3). The synthetic observations $\boldsymbol{u}^{\mathrm{obs}}(\boldsymbol{x}^m)$, $m = 1, 2, \ldots, M$ are generated with the aid of an elastodynamic boundary element method (Pak and Guzina, 1999) by discretizing the surface of the defect via eight-node quadratic elements. The half-space Green's function, required both by the forward solution and by (54), is calculated as in Guzina and Pak (2001). For illustration purposes the results are generated for two excitation frequencies, namely $\bar{\omega} = 1$ and $\bar{\omega} = 4$, where

$$\bar{\omega} = \frac{\omega \, \mathrm{d}}{\sqrt{\mu/\rho}} \equiv 2\pi \frac{d}{\lambda}, \quad \lambda = \frac{2\pi}{\omega} \sqrt{\frac{\mu}{\rho}}, \tag{77}$$

λ being the shear wave length in the reference solid. Here one may note that the wavelength-to-flaw-size ratio, λ/D, is approximately 8 and 2 for $\bar{\omega} = 1$ and $\bar{\omega} = 4$, respectively. In the acoustics literature (Colton and Kress, 1992) such frequencies, where the wave lengths exceed the diameter of the scatterer, are designated as those belonging to the so-called *resonance region*.

As a first illustration, Fig. 4 deals with the case when the material defect is a cavity, and plots the distribution of topological sensitivity in the "horizontal" plane $\xi_3 = 3d$ assuming $\boldsymbol{m} = \boldsymbol{m}^{\mathrm{true}} = (0, 0, 0)$ in (54). For comparison, intersection of the cutting plane with the true defect is indicated in red. One may observe that the regions where $\mathscr{T}_f$ takes pronounced negative values point toward the true effect at both frequencies, albeit in a more localized fashion for $\bar{\omega} = 4$. As examined earlier, such behavior is consistent with an intuitive notion that the points where $\mathscr{T}_f < 0$, and in particular those with marked negative values of $\mathscr{T}_f$, indicate locations where the removal of "excess" material may be most effective as measured by the rate of decrease of $\mathscr{J}_f(\Omega)$ according to (15) and (56).

The next result in Fig. 5 represents a generalization of the first example, this time assuming that the spherical defect is a "stiff" inclusion and calculating the distribution of $\mathscr{T}_f$ with $\boldsymbol{m} = \boldsymbol{m}^{\mathrm{true}} = (5\mu, 0.45, 1.3\rho)$. Notwithstanding the apparent differences in magnitude, the featured $\mathscr{T}_f$-distributions elicit similar comments as those in Fig. 4. For completeness, the "vertical" sections of topological sensitivity (inclusion case) are plotted in Fig. 6 with reference to the plane $\xi_1 = d$ containing the centroid of the defect. Due primarily to a limited aperture of the testing grid, the results reflect a marked drop in the
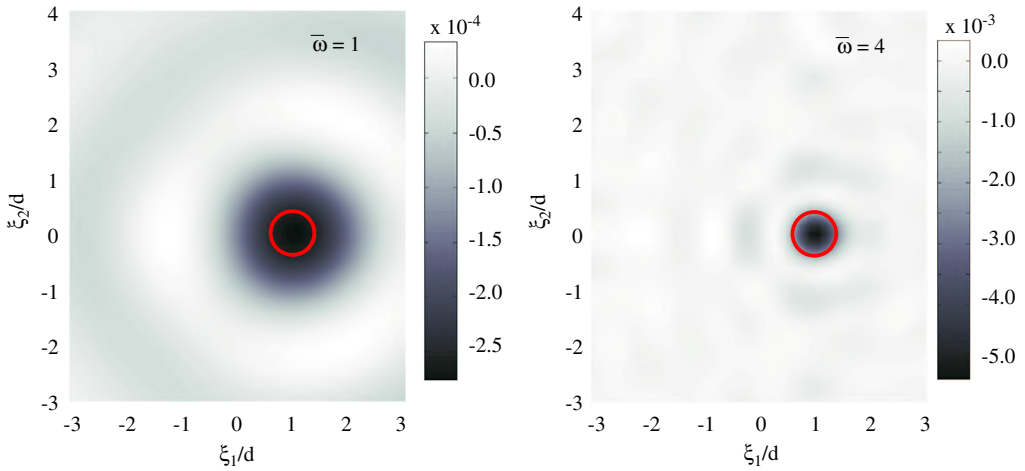
Fig. 4. Cavity defect, $\boldsymbol{m}^{\text{true}} = (0, 0, 0)$: distribution of $\mathcal{T}_f(\boldsymbol{x}^{\text{o}}, \boldsymbol{m}^{\text{true}}) \times d$ in the $\xi_3 = 3d$ plane for $\bar{\omega} = 1$ (left) and $\bar{\omega} = 4$ (right).

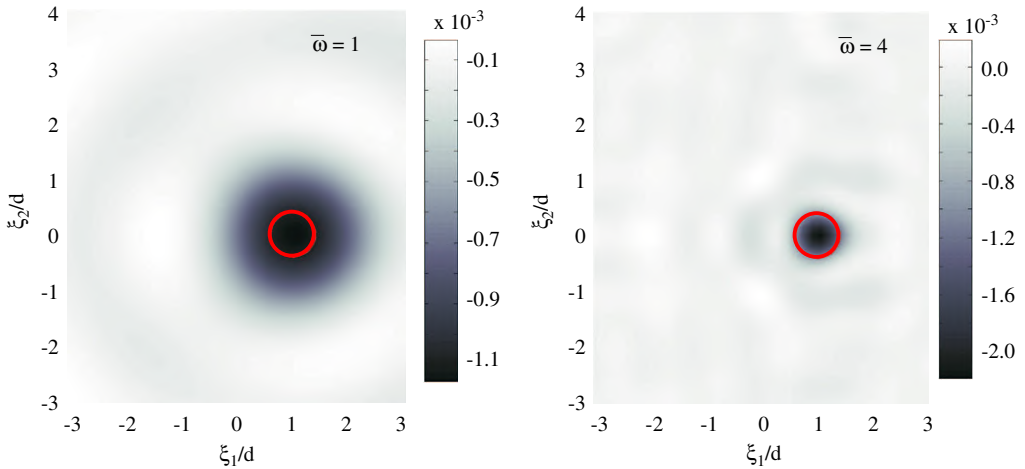Fig. 5. Inclusion defect, $\boldsymbol{m}^{\text{true}} = (5\mu, 0.45, 1.3\rho)$: distribution of $\mathcal{T}_f(\boldsymbol{x}^{\text{o}}, \boldsymbol{m}^{\text{true}}) \times d$ in the $\xi_3 = 3d$ plane for $\bar{\omega} = 1$ (left) and $\bar{\omega} = 4$ (right).

fidelity of subsurface "images", although still furnishing a reasonable information for $\bar{\omega} = 4$.

6.2. Material identification approach

As stipulated earlier, the distributions in Figs. 4–6 are computed assuming full *prior information* about the nature of the defect, manifest in the exact knowledge of the vector $\boldsymbol{m}^{\text{true}} = (\mu^{\star}_{\text{true}}, \nu^{\star}_{\text{true}}, \rho^{\star}_{\text{true}})$. Unfortunately, such information is often unavailable and the question arises whether (54) can be used, through its explicit dependence on $\boldsymbol{m}$ via e.g. (61)
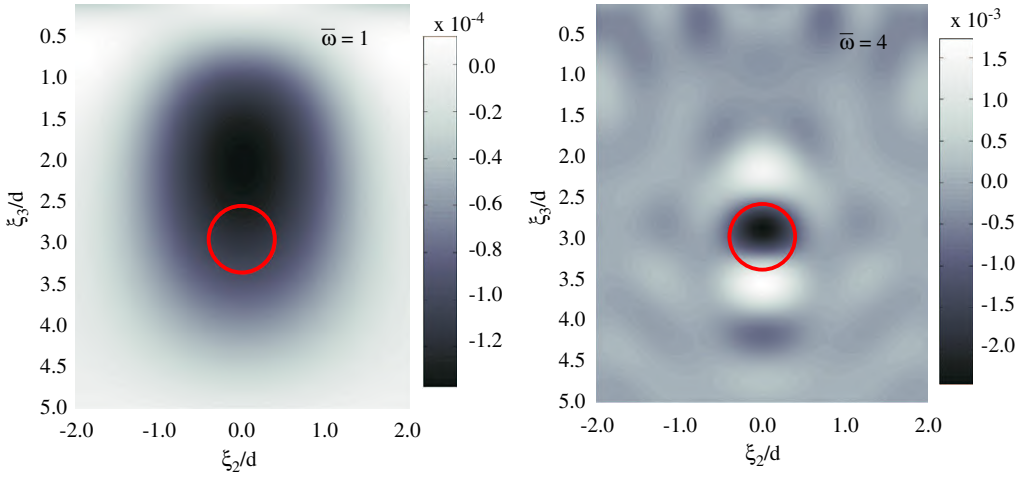
Fig. 6. Inclusion defect, $\boldsymbol{m}^{\text{true}} = (5\mu, 0.45, 1.3\rho)$: distribution of $\mathcal{T}_f(\boldsymbol{x}^{\text{o}}, \boldsymbol{m}^{\text{true}}) \times d$ in the $\xi_1 = d$ plane for $\bar{\omega} = 1$ (left) and $\bar{\omega} = 4$ (right).
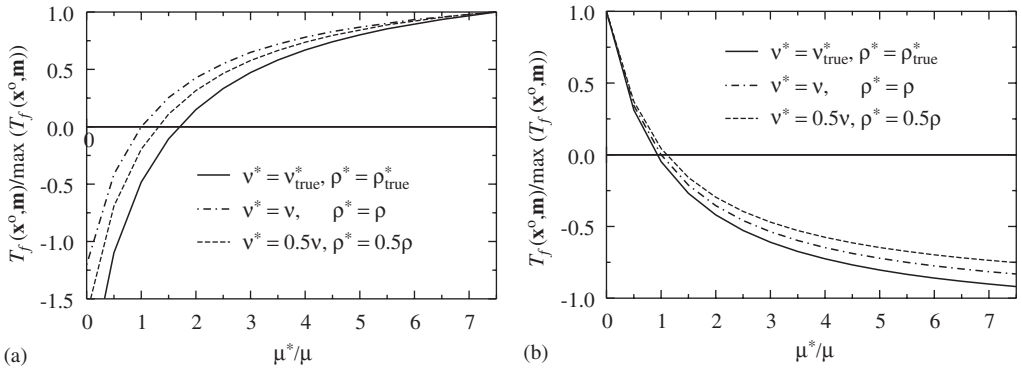
Fig. 7. Variation of $\mathcal{T}_f(\boldsymbol{x}^{\text{o}}, \boldsymbol{m})$ with $m_2 \equiv \mu^{\star}$ at the center of (a) "true" cavity with $\boldsymbol{m}^{\text{true}} = (0, 0, 0)$, and (b) "true" elastic inclusion with $\boldsymbol{m}^{\text{true}} = (5\mu, 0.45, 1.3\rho)$.

and (62), for *both* material and geometric identification of internal defects. To investigate such possibility, Fig. 7 plots the variation of $\mathcal{T}_f(\boldsymbol{x}^{\text{o}}, \boldsymbol{m})$ at the centroid of the "true" spherical defect (namely $\boldsymbol{x}^{\text{o}} = (d, 0, 3d)$) versus the *trial* shear modulus $\mu^{\star}$ for both testing configurations where the material defect is a cavity and "stiff" inclusion, respectively.

From the diagram in Fig. 7a, it is apparent that the band-limited "optimal" value of $\bar{\mu}^{\star} = \mu^{\star}/\mu$ which minimizes $\mathcal{T}_f$, namely $\bar{\mu}^{\star}_{\text{opt}} = 0$, is *consistent* with the shear modulus of the true defect, i.e. $\bar{\mu}^{\star}_{\text{true}} = 0$. A similar comment applies to the diagram in Fig. 7b generated for the stiff defect case ($\bar{\mu}^{\star}_{\text{true}} = 5$), which indicates that the topological sensitivity at $\boldsymbol{x}^{\text{o}} = (d, 0, 3d)$ is minimized by assigning a "high" (band-limited) optimal value of $\bar{\mu}^{\star}_{\text{opt}} = 7.5$ to the nucleating inclusion. In both figures, the relative variation of topological sensitivity was found to depend only mildly on the Poisson's ratio and mass density of the trial obstacle. In view of their consistency, the results in Fig. 7 highlight the potential of

generalized topological sensitivity (54) a tool for both *preliminary* material and geometric identification of internal defects. In this regard, it is noted that the point-wise variation of $\mathscr{T}_f$ is clearly not capable of exposing the exact value of $\bar{\mu}^{\star}_{\text{true}}$. Nonetheless, it has a potential of indicating whether the defect is "stiff" ($\bar{\mu}^{\star}_{\text{true}} > 1$) or "soft" ($\bar{\mu}^{\star}_{\text{true}} < 1$); an information that may be critical for creating a reliable input for more refined, iterative imaging techniques (Bonnet, 1995; Guzina et al., 2003). More practically, such preliminary material information may *by itself* be sufficient to distinguish between the malignant and benign growth in biological tissues (Sarvazyan et al., 1998; Fatemi and Greenleaf, 1998) and thus minimize the need for biopsy.

In the case of a nucleating spherical defect for which tensor $\mathscr{A}$ is given by (61) and (62), the foregoing minimization with respect to $\bar{\mu}^{\star}$ can be performed analytically. In particular, it can be shown that

$$\mu \frac{\partial \mathscr{T}_f}{\partial \bar{\mu}^{\star}}(x^{\text{o}}, m) = -\frac{3(1-v)^2(1+v^{\star})(1-2v^{\star})t_1(x^{\text{o}})}{(1+v)^2\{\bar{\mu}^{\star}(1+v^{\star})+2-4v^{\star}\}^2} - \frac{225(1-v)^2 t_2(x^{\text{o}})}{2\{\bar{\mu}^{\star}(8-10v)+7-5v\}^2},$$

(78)

where the coefficients t_1 and t_2, independent of $\bar{\mu}^{\star}$, are given by

$$t_1(x^{\text{o}}) = \sum_{q=1}^{Q} \int_{\Pi^{\text{obs}}} \text{Re}\left\{\sum_{k=1}^{3} \frac{\partial \varphi}{\partial u_k}(u^{\text{F}}(\xi), u^{\text{obs}})\text{tr}\sigma^{\text{F}}(x^{\text{o}}) \text{ tr } \hat{\sigma}^k(x^{\text{o}}, \xi)\right\}\bigg|_{f=f^q} d\Pi_{\xi},$$

$$t_2(x^{\text{o}}) = \sum_{q=1}^{Q} \int_{\Pi^{\text{obs}}} \text{Re}\left\{\sum_{k=1}^{3} \frac{\partial \varphi}{\partial u_k}(u^{\text{F}}(\xi), u^{\text{obs}})\right.$$

$$\left. \times \left(\sigma^{\text{F}}(x^{\text{o}}) : \hat{\sigma}^k(x^{\text{o}}, \xi) - \frac{1}{3}\text{tr } \sigma^{\text{F}}(x^{\text{o}}) \text{ tr } \hat{\sigma}^k(x^{\text{o}}, \xi)\right)\right\}\bigg|_{f=f^q} d\Pi_{\xi}.$$

(79)

On the basis of (78), the task of finding the extremum of $\mathscr{T}_f(x^{\text{o}}, m)$ can be essentially reduced to solving a *linear equation* in terms of $\bar{\mu}^{\star}$ when $v^{\star}$ and $\rho^{\star}$ are fixed. Depending on the particular values of t_1 and t_2 which combine the experimental data with an information about the free field and the Green's function at x^{o}, however, the latter equation may or may not have physical roots. In particular, if both $t_1(x^o)$ and $t_2(x^o)$ are negative, (78) demonstrates that $\mathscr{T}_f$ is a monotonically increasing function of $\bar{\mu}^{\star}$ so that its (physical) minimum value is reached at $\bar{\mu}^{\star}_{\text{opt}} = 0$. Conversely if both $t_1(x^o)$ and $t_2(x^o)$ are positive, the band-limited minimum of $\mathscr{T}_f$ is reached at $\bar{\mu}^{\star}_{\text{opt}} = \bar{\mu}^{\star}_{\text{max}}$, where $\bar{\mu}^{\star}_{\text{max}}$is the prescribed upper limit of the search range in terms $\bar{\mu}^{\star}$. In the "intermediate" case when $t_1(x^o)\,t_2(x^o) < 0$, on the other hand, $\mathscr{T}_f$ does have an extremum and $\partial\mathscr{T}_f/\partial\bar{\mu}^{\star} = 0$ is reached for $\bar{\mu}^{\star} = \bar{\mu}^{\star}_{\alpha}$ where

$$\bar{\mu}^{\star}_{\alpha} = \frac{\alpha(7-5v)-2+4v^{\star}}{1+v^{\star}-\alpha(8-10v)}, \quad \alpha = \frac{\sqrt{6(1+v^{\star})(1-2v^{\star})}}{15(1+v)}\left|\frac{t_1(x^{\text{o}})}{t_2(x^{\text{o}})}\right|.$$

(80)

On the basis of (80), $\bar{\mu}^{\star}_{\text{opt}}$ takes the value of either $\bar{\mu}^{\star}_{\alpha}$, zero, or $\bar{\mu}^{\star}_{\text{max}}$ chosen so that $\bar{\mu}^{\star}_{\text{opt}} \in [0, \bar{\mu}^{\star}_{\text{max}}]$ and $\mathscr{T}_f|_{\bar{\mu}^{\star}=\bar{\mu}^{\star}_{\text{opt}}} \leqslant \mathscr{T}_f|_{\bar{\mu}^{\star}\in[0,\bar{\mu}^{\star}_{\text{max}}]}$. For clarity, the above discussion is summarized in Table 1. It is also noted from (78) that $\lim_{\bar{\mu}^{\star}\to\infty}\partial\mathscr{T}_f/\partial\bar{\mu}^{\star} = 0$; a result that is reflected in the band-limited variations of $\mathscr{T}_f(x^{\text{o}}, m)$ in Fig. 7 where $t_1(x^o)\,t_2(x^o) > 0$, i.e. there is no extremum in the sense of (80).

In light of the foregoing results, a natural idea geared toward the preliminary (material and geometric) reconstruction of material defects is to introduce a thresholded shear modulus distribution

$$\mathscr{M}(x^{\mathrm{o}}) = \begin{cases} \mu_{\mathrm{opt}}^{\star}, & \mathscr{T}_f(x^{\mathrm{o}}, m^{\mathrm{opt}}) \leqslant c\,\mathscr{T}_f^{\min}, \\ \mu, & \mathscr{T}_f(x^{\mathrm{o}}, m^{\mathrm{opt}}) > c\,\mathscr{T}_f^{\min}. \end{cases} \tag{81}$$

Here $m^{\mathrm{opt}} = (\mu_{\mathrm{opt}}^{\star}, v^{\star}, \rho^{\star})$, where $v^{\star}$ and $\rho^{\star}$ are fixed (i.e. pre-defined) trial values and $\mu_{\mathrm{opt}}^{\star} = \mu\,\bar{\mu}_{\mathrm{opt}}^{\star}$ according to Table 1. For a given sampling region $G \subset \Omega$, $\mathscr{T}_f^{\min} < 0$ is defined as the global minimum, i.e.

$$\mathscr{T}_f^{\min} = \min_{x^{\mathrm{o}} \in G} \mathscr{T}_f(x^{\mathrm{o}}, m^{\mathrm{opt}}),$$

whereas $0 < c < 1$ is a suitable threshold value. From Figs. 4–6, it appears that the distribution of generalized topological sensitivity tends to be more "smeared" at lower frequencies, a conclusion that is consistent with earlier studies (Guzina and Bonnet, 2004; Bonnet and Guzina, 2004). Accordingly, one may select a threshold value that is more restrictive at lower frequencies (i.e. longer excitation wavelengths λ), e.g.

$$c = c(\bar{\omega}) = C(1 + \bar{\omega}^{-1}), \quad C = \mathrm{const.} \tag{82}$$

With reference to the topological sensitivity formula (54), it is worth noting that the excitation frequency plays no role in the calculation of tensor $\mathscr{A}$ that is obtained through a limiting process as $a \to 0$ with ω fixed so that $a/\lambda \to 0$ as well. In contrast, the ratios between other characteristic lengths of the problem (e.g. depth to the obstacle, true defect size, depth of the sampling point, size of the testing grid) and the excitation wavelength λ do have an effect on $\mathscr{T}$ as they impact: (i) the observed data u^{obs}, (ii) the free field (u^{F}, σ^{F}), and (iii) the Green's function values ($\hat{u}^k$, $\hat{\sigma}^k$). In principle, the effect of decreasing λ (or increasing ω) on $\mathscr{T}$ in (54) is such that it leads to more rapid fluctuations e.g. in terms of $\hat{u}^k(x^{\mathrm{o}}, \cdot)$ and $u^{\mathrm{F}}(x^{\mathrm{o}})$ and consequently to a more localized distribution of topological sensitivity. In the support of this argument, a careful inspection of the results in Figs. 4 and 5 reveals the presence a barely visible "halo", with diameter $\approx \lambda$, that surrounds the true obstacle for both $\bar{\omega} = 1$ and 4.

Throughout the remainder of this paper, the default values of $v^{\star} = v$, $\rho^{\star} = 0.5\rho$ and $C = 0.45$ are used as an example. Here it is noted that the reasons for the particular choice of $\rho^{\star}$ are twofold: (i) taking $\rho^{\star} = \rho$ would artificially delete the monopole term in (54), and (ii) $\rho^{\star} = 0.5\rho$ can be considered as an intermediate value between the extreme cases of a cavity ($\rho_{\mathrm{true}}^{\star} = 0$) and a "heavy" inclusion ($\rho_{\mathrm{true}}^{\star} > 1$), see also Fig. 7.

The performance of (81) is illustrated in Figs. 8 and 9 dealing with the cases when the material defect is a cavity and "stiff" inclusion, respectively. To provide a basis

Table 1
Spherical defect: dependence of $\bar{\mu}_{\mathrm{opt}}^{\star}$ on t_1 and t_2 at the sampling point

$\bar{\mu}_{\mathrm{opt}}^{\star}$	$t_1(x^{\mathrm{o}}) < 0$	$t_1(x^{\mathrm{o}}) > 0$
$t_2(x^{\mathrm{o}}) < 0$	$\bar{\mu}_{\mathrm{opt}}^{\star} = 0$	$\bar{\mu}_{\mathrm{opt}}^{\star} \in \{\bar{\mu}_{\alpha}^{\star}, 0, \bar{\mu}_{\max}^{\star}\}$
$t_2(x^{\mathrm{o}}) > 0$	$\bar{\mu}_{\mathrm{opt}}^{\star} \in \{\bar{\mu}_{\alpha}^{\star}, 0, \bar{\mu}_{\max}^{\star}\}$	$\bar{\mu}_{\mathrm{opt}}^{\star} = \bar{\mu}_{\max}^{\star}$

Fig. 8. Cavity defect, $\boldsymbol{m}^{\text{true}} = (0, 0, 0)$: distribution of $\mathcal{M}(\boldsymbol{x}^{\text{o}})/\mu$ in the $\xi_3 = 3d$ plane for $\bar{\omega} = 1$ (left) and $\bar{\omega} = 4$ (right).
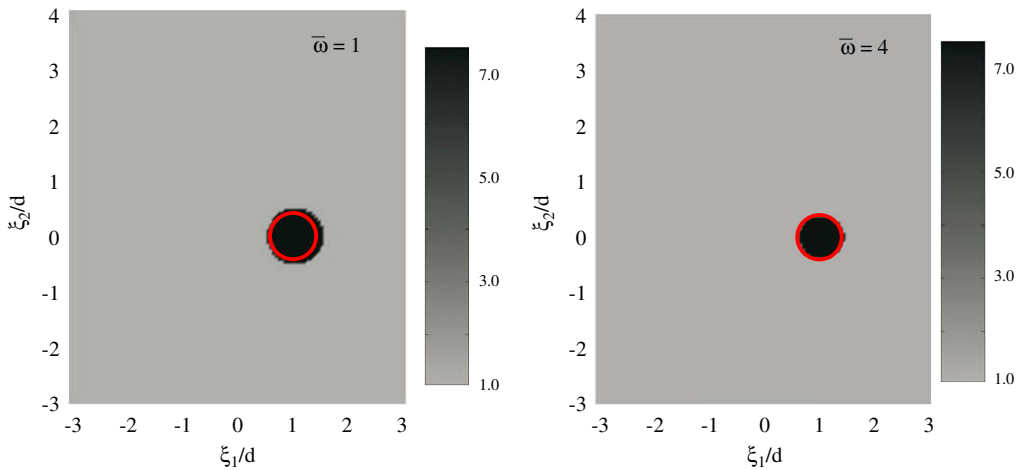

Fig. 9. Inclusion defect, $\boldsymbol{m}^{\text{true}} = (5\mu, 0.45, 1.3\rho)$: distribution of $\mathcal{M}(\boldsymbol{x}^{\text{o}})/\mu$ in the $\xi_3 = 3d$ plane for $\bar{\omega} = 1$ (left) and $\bar{\omega} = 4$ (right).

for comparison, intersection of the "true" defect with the cutting plane is again indicated in red. The results support the notion that the generalized topological sensitivity (54), which postulates the nucleation of a solid inclusion, may provide reliable *preliminary* information about both geometry and material characteristics of an obstacle through the distribution of $\mathcal{M}(\boldsymbol{x}^{\text{o}})$. With reference to Table 1, it is worth mentioning that the case most commonly encountered in Figs. 8, 9 and thereafter is that where $t_1(\boldsymbol{x}^{\text{o}}) t_2(\boldsymbol{x}^{\text{o}}) > 0$ so that $\bar{\mu}_{\text{opt}}^{\star}$ is either zero or $\bar{\mu}_{\text{max}}^{\star}$ for the majority of sampling points.

6.3. Multiple defects

To examine the applicability of the foregoing developments to more complex situations involving multiple defects, consider the testing arrangement as in Fig. 3 ($v = 0.3$) in conjunction with a dual-obstacle configuration. Here, the first defect is a spherical cavity of diameter $0.8d$, located at $(-2d, -2d, 3d)$ inside the half-space; the second defect is a "stiff" ellipsoidal inclusion, centered at $(1.5d, 1.5d, 3d)$, with axes $(1.6d, 0.4d, 1.2d)$ aligned with the reference Cartesian frame. Material properties of the inclusion are taken as $\boldsymbol{m}^{\text{true}} = (5\mu, 0.45, 1.3\rho)$.

As a first illustration, the spatial distribution of $\mathcal{T}_f(\boldsymbol{x}^\circ, \boldsymbol{0})$ in the horizontal plane $\xi_3 = 3d$ for the dual-obstacle problem is shown in Fig. 10. Clearly such "conventional" topological sensitivity, that postulates the nucleation an infinitesimal cavity (i.e. $\boldsymbol{m} = \boldsymbol{0}$), fails to identify the ellipsoidal inclusion through regions where $\mathcal{T}_f < 0$. In fact, $\mathcal{T}_f(\boldsymbol{x}^\circ, \boldsymbol{0})$ for the problem of interest takes extreme *positive* values the neighborhood of the ellipsoidal inclusion. In contrast, the distribution of $\mathcal{T}_f(\boldsymbol{x}^\circ, \boldsymbol{m}^{\text{opt}})$ in Fig. 11 identifies both the cavity and inclusion through marked negative values of $\mathcal{T}_f$. As examined earlier, $\boldsymbol{m}^{\text{opt}} = (\mu^\star_{\text{opt}}, v^\star, \rho^\star)$ where $v^\star$ and $\rho^\star$ are fixed trial values (set respectively to v and 0.5ρ as an example) and $\mu^\star_{\text{opt}}$ is the band-limited optimal value of $\mu^\star$ minimizing $\mathcal{T}_f$ at $\boldsymbol{x}^\circ$. To provide a more definitive information about the two defects, Fig. 12 plots the distribution of the thresholded shear modulus $\mathcal{M}$ according to (81) applied to the neighborhood of each local minimum. As can be seen from the display, the $\mathcal{M}$-distributions at both frequencies correctly identify the "left" and "right" defect as a cavity and stiff inclusion, respectively.

To cater for engineering applications, it is noted with reference to (77) that the ratio between the centroidal flaw distance L and the excitation wavelength λ in Figs. 10–12 equals approximately 0.8 and 3.2 for $\bar{\omega} = 1$ and $\bar{\omega} = 4$, respectively. Additional simulations have shown that the $\mathcal{T}_f$-distribution is characterized by a diminished accuracy for L/λ ratios less than approximately 0.4. As an illustration, Fig. 13 shows one such example where the "true" ellipsoidal inclusion is placed closer to the spherical cavity so that $L/\lambda \approx 0.3$.
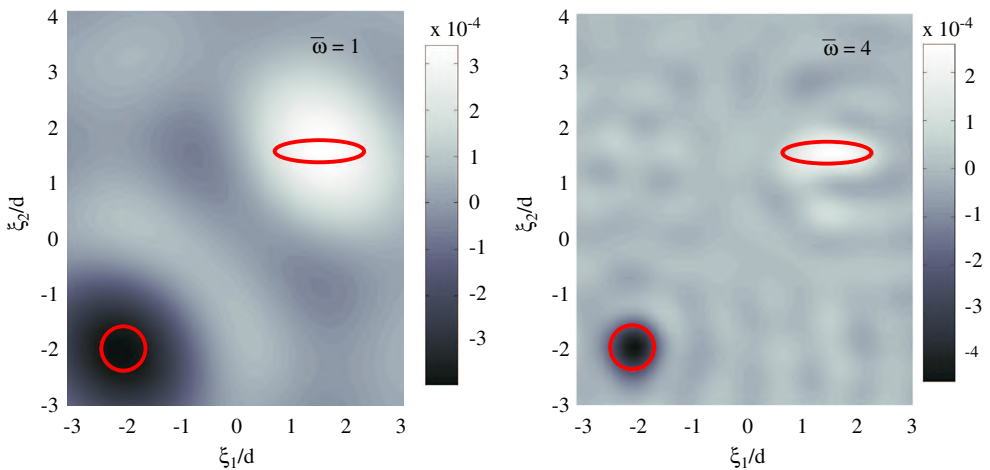

Fig. 10. Dual defects: distribution of $\mathcal{T}_f(\boldsymbol{x}^\circ, \boldsymbol{0}) \times d$ in the $\xi_3 = 3d$ plane for $\bar{\omega} = 1$ (left) and $\bar{\omega} = 4$ (right).

Fig. 11. Dual defects: distribution of $\mathcal{T}_f(\boldsymbol{x}^o, \boldsymbol{m}^{opt}) \times d$ in the $\xi_3 = 3d$ plane for $\bar{\omega} = 1$ (left) and $\bar{\omega} = 4$ (right).

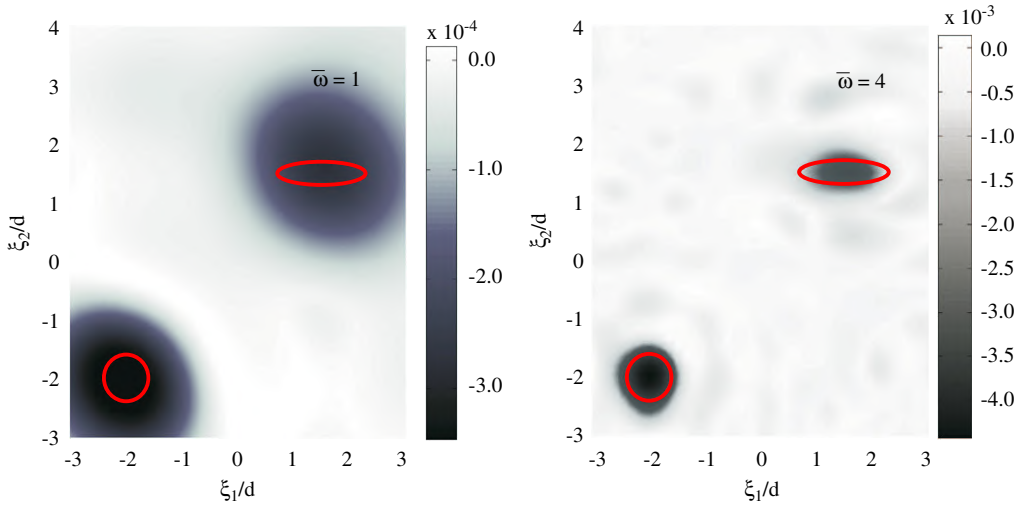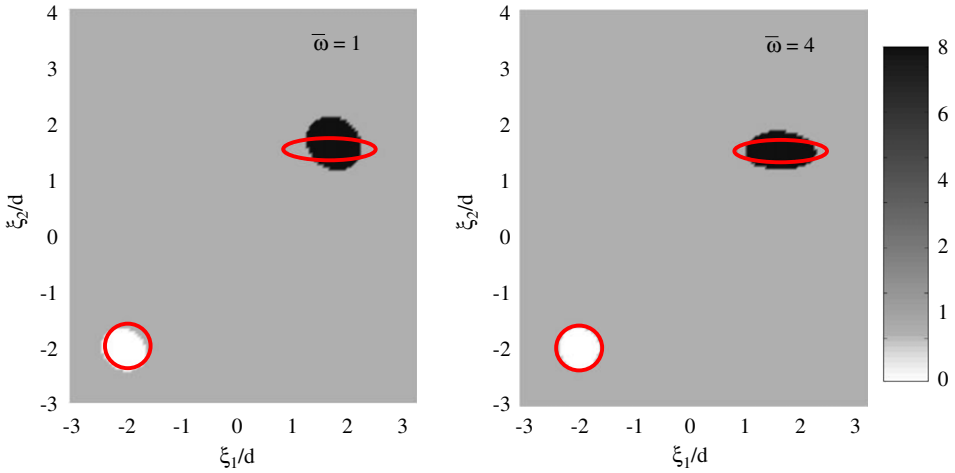Fig. 12. Dual defects: distribution of $\mathcal{M}(\boldsymbol{x}^o)/\mu$ in the $\xi_3 = 3d$ plane for $\bar{\omega} = 1$ (left) and $\bar{\omega} = 4$ (right).

6.4. Functionally graded materials

From the asymptotic analysis in Section 4, it follows that sensitivity formula (54) applies to *any* reference (i.e. background) solid Ω for which

- elastodynamic Green's function ($\hat{\boldsymbol{u}}^k$ and $\hat{\boldsymbol{t}}^k$, $k \in \{1, 2, 3\}$) is available, and
- $\hat{\boldsymbol{u}}^k$ and $\hat{\boldsymbol{t}}^k$ permit decomposition (31) where the singular parts $[\hat{\boldsymbol{u}}^k]_1$ and $[\hat{\boldsymbol{t}}^k]_1$ are given by the (elastostatic) Kelvin's solution.
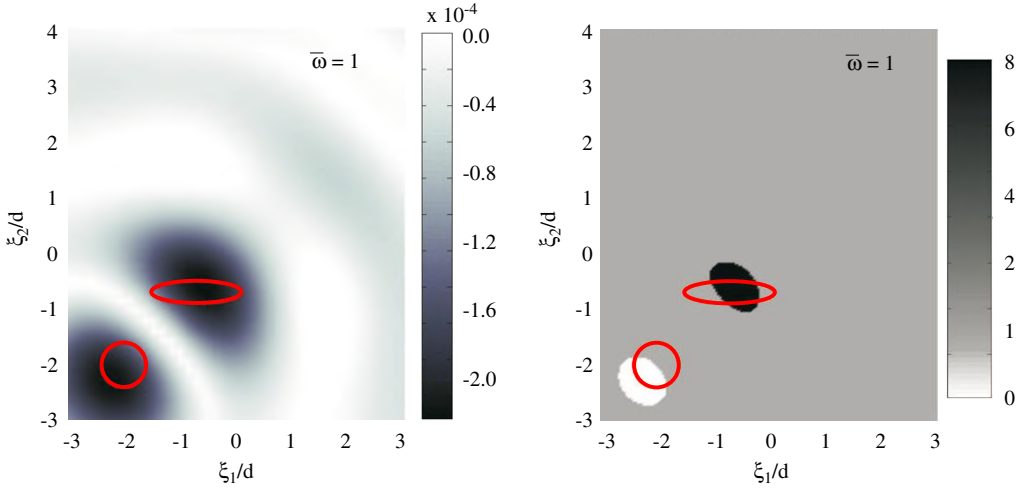
Fig. 13. Dual defects, proximate obstacle configuration: distribution of $\mathscr{T}_f(\mathbf{x}^\text{o}, \mathbf{m}^\text{opt}) \times d$ (left) and $\mathscr{M}(\mathbf{x}^\text{o})/\mu$ (right) in the $\xi_3 = 3d$ plane.

In Pak and Guzina (1995) and Guzina and Pak (1996), the displacement component $\hat{u}^k$ of the Green's function was developed for the class of functionally-graded, semi-infinite solids $\Omega = \{(\xi_1, \xi_2, \xi_3) \mid \xi_3 > 0\}$ with continuous variation of Lamé parameters according to

$$\mu(z) = \mu_o(1 + b\,\xi_3)^2, \quad v = 0.25, \quad \rho = \text{const.}, \tag{83}$$

where ξ_3 is the direction of grading. In particular, it was shown (Guzina and Pak, 1996) that $\hat{\mathbf{u}}^k(\boldsymbol{\xi}, \mathbf{x})$ satisfies (31) where $[\hat{\mathbf{u}}^k]_1$ is given by the Kelvin's solution with $\mu = \mu_0(1 + b\,\mathbf{x} \cdot \mathbf{e}_3)^2$ and $v = 0.25$. In Guzina and Chikichev (in preparation), these findings were recently extended in terms of their traction counterparts, $\hat{\mathbf{t}}^k$, which makes the graded materials of class (83) amenable to preliminary imaging in terms of (54). To examine the latter possibility, consider the testing arrangement described earlier (Fig. 3) as applied to the functionally graded material (83) with $b = 0.2/d$ and a cavity of diameter $0.8d$ centered at $(d, 0, 3d)$. For brevity, the results are shown for a single excitation frequency, $\bar{\omega} \equiv \omega\,d/\sqrt{\mu_o/\rho} = 4$. The left diagram in Fig. 14 plots the distribution of $\mathscr{T}_f(\mathbf{x}^\text{o}, \mathbf{m}^\text{opt})$ in the "horizontal" plane $\xi_3 = 3d$ containing the centroid of the defect. For completeness, the right diagram plots the corresponding distribution of the thresholded shear modulus (81) where $\mu = \mu(\mathbf{x}^\text{o} \cdot \mathbf{e}_3)$ varies with depth according to (83). Here $v^\star = v$, $\rho^\star = 0.5\rho$, and $C = 0.45$ as prescribed earlier. Notwithstanding the apparent differences in the nature of respective background media, the fidelity of images in Fig. 14 is indeed similar to that of their homogeneous-matrix counterparts in Figs. 4 and 8. Consistent with the earlier findings, the "vertical-slice" images of the void defect (in terms of $\mathscr{M}$) in Fig. 15 are still reasonable although of lower quality than that in Fig. 14.

6.5. Multi-tonal illumination

In the preceding examples, a preliminary information about the size of the defect stemming from (54) can be seen to clearly depend on the assumed threshold value,
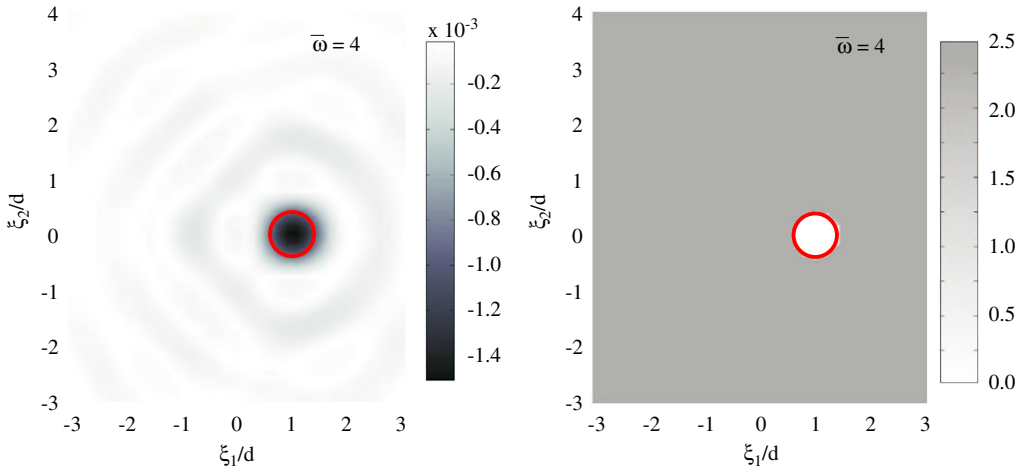
Fig. 14. Functionally graded material: distribution of $\mathcal{T}_f(x^o, m^{opt}) \times d$ (left) and $\mathcal{M}(x^o)/\mu$ (right) in the $\xi_3 = 3d$ plane for $\bar{\omega} = 4$.
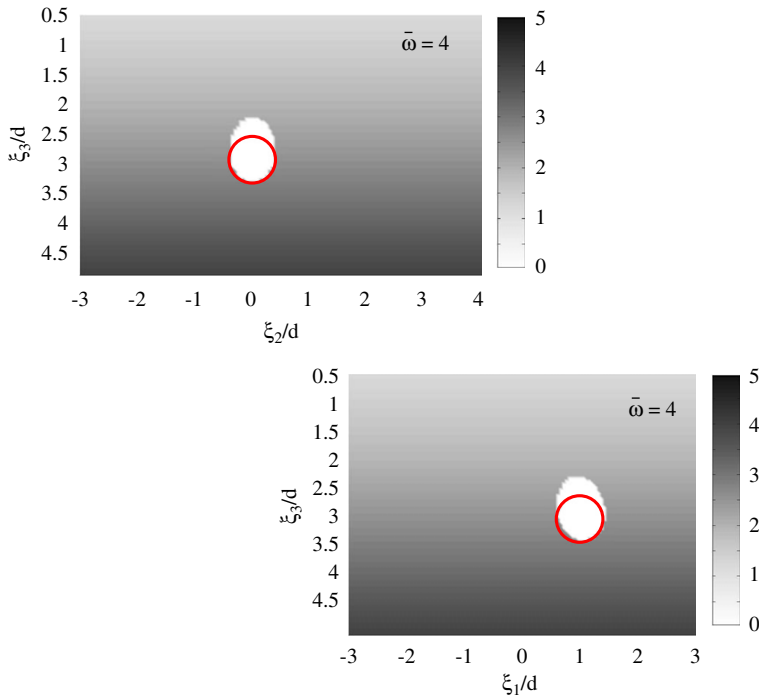

Fig. 15. Functionally graded material: distribution of $\mathcal{M}(x^o)/\mu_o$ in the $\xi_1 = d$ plane (top) and $\xi_2 = 0$ plane (bottom) for $\bar{\omega} = 4$.

$c = c(\bar{\omega})$, via (81). To transcend such impediment, one may consider the higher-order terms in expansion (15) that would inherently carry an additional information about the (size of the) defect. Another possibility, examined in this study, is to employ multiple

"illuminating" frequencies as a source of such additional information. To this end consider the testing configuration in Fig. 4, this time with reference to a homogeneous *full-space* with shear modulus μ, Poisson's ratio v and mass density ρ. The infinite solid contains an ellipsoidal void, centered at $(1d, 0d, 3d)$, whose axes $(1.6d, 0.8d, 1.2d)$ are aligned with the reference Cartesian frame. Apart from its direct relevance to medical imaging owing to (i) high attenuation rate for shear waves in biological tissues (which allows the boundary reflections to be neglected) and (ii) the ability of confocal ultrasound beams to apply internal "point" loads (Fatemi and Greenleaf, 1998), the infinite background was chosen for its closed-form Green's function which permits efficient calculations at "high" frequencies (in this example $\bar{\omega} = 8$). As an example, the first three graphs (top row and left column) in Fig. 16 plot the distribution of $\mathscr{T}_f(\mathbf{x}^\circ, \mathbf{m}^{\text{true}})$ in the $\xi_3 = 3d$ plane for illuminating frequencies $\bar{\omega} = 2, 4$ and 8. Illustrating the featured idea of multi-tonal imaging, the bottom right diagram in Fig. 16 plots the combined multi-tonal information $\Pi_{k=1}^{3} \min\{0, \mathscr{T}_f(\mathbf{x}^\circ, \mathbf{m}^{\text{true}})|_{\bar{\omega}=2^k}\}$ obtained using the negative values of $\mathscr{T}_f$ at $\bar{\omega} = 2, 4, 8$. As can be seen from the display, the hybrid image reasonably traces the outline of the defect using only the *trivial* threshold value of zero at all frequencies.
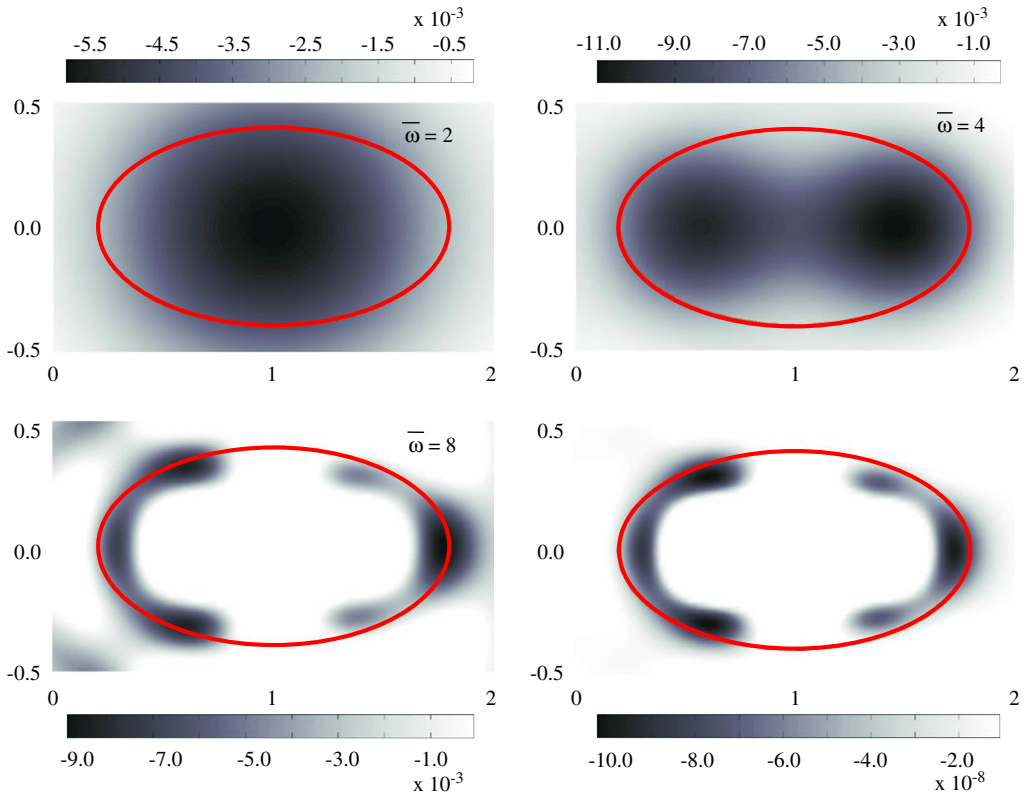

Fig. 16. Distribution of $\mathscr{T}_f(\mathbf{x}^\circ, \mathbf{m}^{\text{true}})$ across plane $\xi_3 = 3d$: $\bar{\omega} = 2$ (top left), $\bar{\omega} = 4$, (top right) $\bar{\omega} = 8$ (bottom left), and $\Pi_{k=1}^{3} \min\{0, \mathscr{T}_f(\mathbf{x}^\circ, \mathbf{m}^{\text{true}})|_{\bar{\omega}=2^k}\}$ (bottom right).

6.6. Effect of shape of the nucleating defect

In Sections 4 and 5, the generalized topological sensitivity in (54) and (74) is shown to depend on the shape and elastic parameters of the nucleating defect via the fourth-order tensor $\mathscr{A}(\boldsymbol{m})$. As stipulated earlier, the results in Figs. 4–16 are all generated on the basis of an assumption that the nucleating obstacle is spherical for which $\mathscr{A}$ permits closed-form representation in terms of (61) and (62). Prompted by the availability of explicit expression (60) that characterizes $\mathscr{A}$ when the reference region $\mathscr{B}$ is ellipsoidal, Fig. 17 illustrates the effect of the shape of $\mathscr{B}$ on the $\mathscr{T}_f$-distribution for the cavity-in-a-homogeneous-half-space problem examined earlier in Fig. 4. In the display, the $\mathscr{B}$-shapes compared are: (i) the sphere, generated as an ellipsoid with axes (d, d, d); (ii) a "generic" ellipsoid with axes $(3d, 2d, d)$, and (iii) a penny-shaped defect, constructed as a degenerate ellipsoid with axes $(3d, 3d, 0.003d)$. In all cases, the principal axes of $\mathscr{B}$ are aligned with the reference
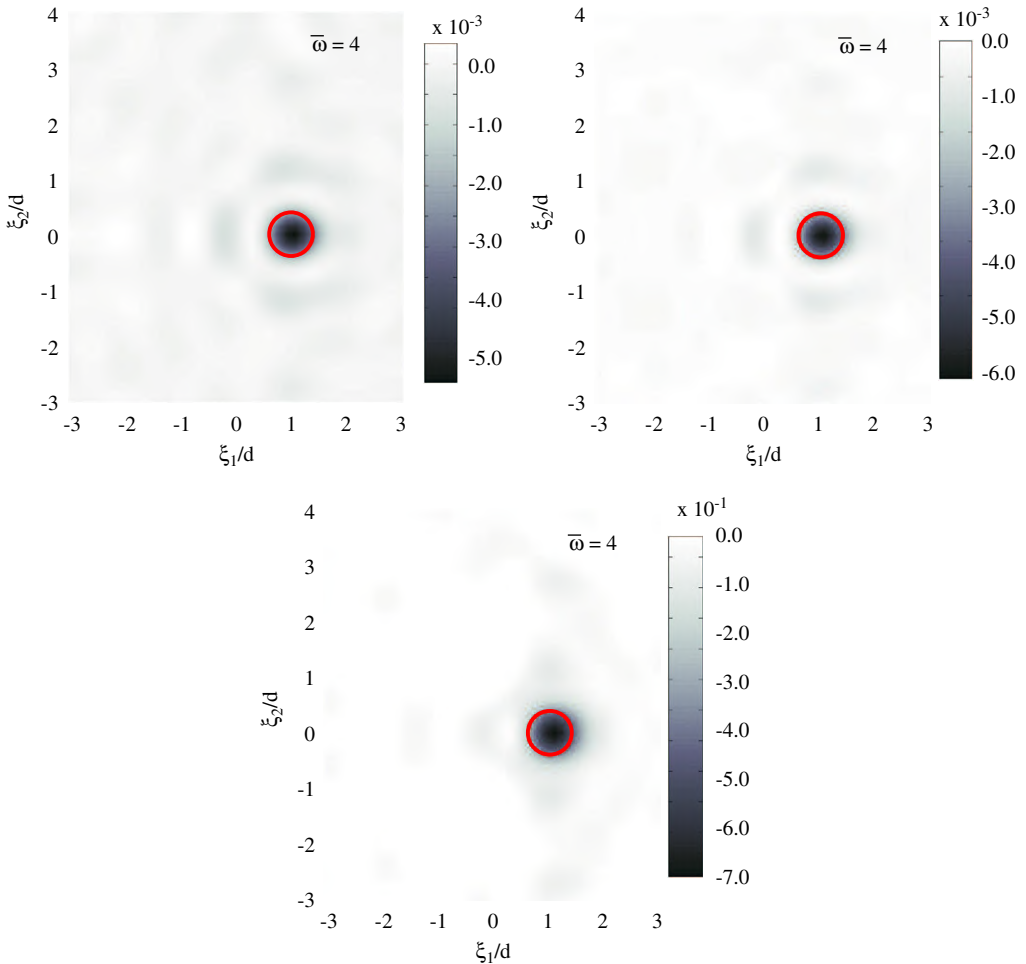

Fig. 17. Cavity defect, $\boldsymbol{m}^{\text{true}} = (0, 0, 0)$: distribution of $\mathscr{T}_f(\boldsymbol{x}^\circ, \boldsymbol{m}^{\text{true}}) \times d$ in the $\xi_3 = 3d$ plane for $\bar{\omega} = 4$ when $\mathscr{B}$ is spherical (top left), ellipsoidal (top right), and penny-shaped (bottom).

Cartesian system. As can be seen from the graphs, the shape of $\mathcal{B}$ does have an effect on the overall distribution and magnitude of $\mathcal{T}_f$, although it does not appear to be essential for the fidelity of geometric (obstacle) identification. It is expected, however, that the shape of $\mathcal{B}$ will be more critical for the higher-order terms in expansion (15); an item that is beyond the scope of this study.

7. Conclusions

In this study the concept of topological derivative, that has its origins in elastostatics and structural shape optimization, is extended to permit preliminary, yet robust 3D elastic-wave identification of material defects. In a departure from earlier studies that revolve around the idea of cavity nucleation, the proposed approach postulates the creation of an (infinitesimal) elastic inclusion. On taking the limit of a boundary integral representation of the scattered field caused by an elastic defect with diminishing size, a generalized formula for topological derivative, which embodies the material parameters of both the matrix and the defect, is formulated explicitly in terms of the elastodynamic Green's function for the reference (defect-free) solid. In the context of arbitrarily shaped inclusions, the formula was shown to consist of a dipole and a monopole term, related respectively to the elasticity and mass density contrasts between the nucleating obstacle and a background medium. To deal with situations (e.g. finite reference bodies) where the prerequisite Green's function is unavailable, an alternative expression for topological sensitivity is obtained via the adjoint field approach that involves a contraction of two (numerically-computed) elastodynamic states. Through a set of numerical examples involving frequencies in the so-called resonance region (wavelengths longer than the size of a defect), the generalized topological sensitivity is shown to be an effective tool for preliminary material identification of subsurface defects through a *point-wise* identification of "optimal" inclusion properties that minimize the topological sensitivity at a sampling location. The results for homogeneous and functionally-graded reference materials indicate that the complementary 3D information about the defect geometry could be obtained with the aid of either (i) a suitable threshold value, or (ii) using multi-tonal illumination, especially that involving "high" frequencies (i.e. those exceeding the resonance region). Beyond the realm of non-destructive material testing, the proposed developments may be relevant to medical diagnosis and in particular to breast cancer detection where focused ultrasound waves show a promise of superseding manual palpation.

Acknowledgments

Appendix A

A.1. Tensors $\mathcal{V}$ and $\mathcal{Q}$ for the reference ellipsoidal inclusion

Consider an infinite elastic solid, housing an ellipsoidal inclusion $\mathcal{B}$, that is subject to a constant state of stress (σ^∞) at infinity. The elastic "matrix" is characterized by the shear

modulus μ and Poisson's ratio v; the respective material properties of the defect, centered at the origin of the reference Cartesian frame $\{O; \xi_1, \xi_2, \xi_3\}$, are denoted by $\mu^\star$ and $v^\star$. With the assumption of a bonded contact between the defect and the matrix, the displacement field within the inclusion, $\overset{\star}{\boldsymbol{\vartheta}}$, and its "exterior" counterpart $\boldsymbol{\vartheta}$ are governed by the field equations and boundary conditions

$$\nabla \cdot (\boldsymbol{C} : \nabla \boldsymbol{\vartheta}) = \boldsymbol{0}, \quad \zeta \in \mathbb{R}^3 \backslash \bar{\mathscr{B}},$$

$$\nabla \cdot (\boldsymbol{C}^\star : \nabla \overset{\star}{\boldsymbol{\vartheta}}) = \boldsymbol{0}, \quad \zeta \in \mathscr{B},$$

$$\boldsymbol{\vartheta} = \overset{\star}{\boldsymbol{\vartheta}}, \quad \boldsymbol{\eta} \cdot (\boldsymbol{C} : \nabla \boldsymbol{\vartheta} - \boldsymbol{C}^\star : \nabla \overset{\star}{\boldsymbol{\vartheta}}) = \boldsymbol{0}, \quad \zeta \in \mathscr{S},$$

$$\lim_{|\zeta| \to \infty} (\boldsymbol{C} : \nabla \boldsymbol{\vartheta} - \boldsymbol{\sigma}^\infty) = \boldsymbol{0}, \tag{A.1}$$

where $\boldsymbol{C}$ and $\boldsymbol{C}^\star$ are given by (2), and $\boldsymbol{\eta}$ is the unit normal on $\mathscr{S} = \partial \mathscr{B}$ oriented toward the interior of $\mathscr{B}$. For the ensuing developments, it is useful to introduce the an auxiliary quantity $\tilde{\boldsymbol{\vartheta}}$, termed the *perturbation* displacement field, through the decomposition

$$\tilde{\boldsymbol{\vartheta}}(\zeta) = \begin{cases} \boldsymbol{\vartheta}(\zeta) - \boldsymbol{D} : \boldsymbol{\sigma}^\infty \cdot \zeta, & \zeta \in \mathbb{R}^3 \backslash \bar{\mathscr{B}}, \\ \overset{\star}{\boldsymbol{\vartheta}}(\zeta) - \boldsymbol{D} : \boldsymbol{\sigma}^\infty \cdot \zeta, & \zeta \in \bar{\mathscr{B}}, \end{cases} \tag{A.2}$$

applied both outside and inside the obstacle. Here it is noted that precluding rigid-body rotation, the linear term $\boldsymbol{D} : \boldsymbol{\sigma}^\infty \cdot \zeta$ signifies the displacement in a defect-free matrix due to constant stress at infinity. By virtue of (A.2), system (A.1) is identified with the elastostatic transmission problem (41) provided that

$$\boldsymbol{\sigma}^\infty = \boldsymbol{\sigma}^{\mathrm{F}}(\boldsymbol{x}^\circ).$$

To solve (A.1) via the equivalent-eigenstrain method (Mura, 1987), let $\boldsymbol{\varepsilon}^\infty = \boldsymbol{D} : \boldsymbol{\sigma}^\infty$ denote the constant strain at infinity corresponding to $\boldsymbol{\sigma}^\infty$, and let $\tilde{\boldsymbol{\varepsilon}}$ and $\tilde{\boldsymbol{\sigma}}$ denote the respective perturbations of $\boldsymbol{\varepsilon}^\infty$ and $\boldsymbol{\sigma}^\infty$ in $\mathbb{R}^3$ due to a presence of the defect. With such decomposition, the total stress and strain fields in $\mathbb{R}^3$ can be respectively written as $\boldsymbol{\sigma}^\infty + \tilde{\boldsymbol{\sigma}}$ and $\boldsymbol{\varepsilon}^\infty + \tilde{\boldsymbol{\varepsilon}}$ so that

$$\boldsymbol{\sigma}^\infty + \tilde{\boldsymbol{\sigma}} = \begin{cases} \boldsymbol{C} : (\boldsymbol{\varepsilon}^\infty + \tilde{\boldsymbol{\varepsilon}}), & \zeta \in \mathbb{R}^3 \backslash \mathscr{B}, \\ \boldsymbol{C}^\star : (\boldsymbol{\varepsilon}^\infty + \tilde{\boldsymbol{\varepsilon}}), & \zeta \in \mathscr{B}. \end{cases} \tag{A.3}$$

Following Eshelby (1957), mechanical effects of the ellipsoidal inclusion in (A.1) can be simulated by an introduction of an equivalent eigenstrain $\boldsymbol{\varepsilon}$ over $\mathscr{B}$ in the unperturbed, i.e. defect-free solid $\mathbb{R}^3$. In other words, one seeks $\boldsymbol{\varepsilon}$ such that the total stress, $\boldsymbol{\sigma}^\infty + \tilde{\boldsymbol{\sigma}}$, inside $\mathscr{B}$ can be computed as

$$\boldsymbol{C}^\star : \nabla \overset{\star}{\boldsymbol{\vartheta}} = \boldsymbol{C}^\star : (\boldsymbol{\varepsilon}^\infty + \tilde{\boldsymbol{\varepsilon}}) = \boldsymbol{C} : (\boldsymbol{\varepsilon}^\infty + \tilde{\boldsymbol{\varepsilon}} - \boldsymbol{\varepsilon}), \quad \zeta \in \mathscr{B}. \tag{A.4}$$

For a uniform stress $\boldsymbol{\sigma}^\infty$, the eigenstrain $\boldsymbol{\varepsilon}$ is also uniform (Eshelby, 1957) and can be related to the perturbation stain through

$$\tilde{\boldsymbol{\varepsilon}} = \mathscr{S} : \boldsymbol{\varepsilon}, \quad \zeta \in \mathscr{B}, \tag{A.5}$$

where $\mathscr{S}$ is the (constant fourth-order) Eshelby tensor whose explicit formulas are available e.g. in Mura (1987). From (A.4), (A.5) and the relationship $\boldsymbol{\varepsilon}^\infty = \boldsymbol{D} : \boldsymbol{\sigma}^\infty$,

one finds

$$\boldsymbol{\varepsilon} = \mathscr{R} : \boldsymbol{\sigma}^\infty, \quad \mathscr{R} \equiv [(\boldsymbol{C} - \boldsymbol{C}^\star) : \mathscr{S} - \boldsymbol{C}]^{-1} : (\boldsymbol{C}^\star - \boldsymbol{C}) : \boldsymbol{D}, \tag{A.6}$$

where, for a fourth-order tensor $\mathscr{T}$ with minor symmetries ($\mathscr{T}_{ijkl} = \mathscr{T}_{jikl} = \mathscr{T}_{ijlk}$),

$$\mathscr{T} : \mathscr{T}^{-1} = \mathscr{T}^{-1} : \mathscr{T} = \boldsymbol{I}_4, \tag{A.7}$$

see Dahlquist and Bjorck (1974). Here $\boldsymbol{I}_4 = \frac{1}{2}(\delta_{ik}\delta_{jl} + \delta_{il}\delta_{jk})\boldsymbol{e}_i \otimes \boldsymbol{e}_j \otimes \boldsymbol{e}_k \otimes \boldsymbol{e}_l$ denotes the symmetric fourth-order identity tensor introduced earlier. On denoting

$$\mathscr{T} = (\boldsymbol{C} - \boldsymbol{C}^\star) : \mathscr{S} - \boldsymbol{C}, \tag{A.8}$$

it can be shown that $\mathscr{T} = \mathscr{T}_{ijkl}\,\boldsymbol{e}_i \otimes \boldsymbol{e}_j \otimes \boldsymbol{e}_k \otimes \boldsymbol{e}_l$ has same structure as tensor $\mathscr{S}$, i.e. that it has 21 non-zero components with $\mathscr{T}_{ijkl} = 0 \Leftrightarrow \mathscr{S}_{ijkl} = 0$ ($i, j, k, l = 1, 2, 3$) when both $\boldsymbol{C}$ and $\boldsymbol{C}^\star$ are isotropic as postulated in (2). By solving the linear system stemming from (A.7) and (A.8), one can further demonstrate that the components of $\mathscr{T}^{-1} \equiv \mathscr{T}_{ijkl}^{-1}\,\boldsymbol{e}_i \otimes \boldsymbol{e}_j \otimes \boldsymbol{e}_k \otimes \boldsymbol{e}_l$ are given by

$$\mathscr{T}_{ijkl}^{-1} = \mathscr{T}_{jikl}^{-1} = \mathscr{T}_{ijlk}^{-1}, \quad \mathscr{T}_{1212}^{-1} = \frac{1}{4\mathscr{T}_{1212}}, \quad \mathscr{T}_{1111}^{-1} = \frac{1}{\mathscr{D}}(\mathscr{T}_{2222}\mathscr{T}_{3333} - \mathscr{T}_{2233}\mathscr{T}_{3322}),$$

$$\mathscr{T}_{1122}^{-1} = \frac{1}{\mathscr{D}}(\mathscr{T}_{1133}\mathscr{T}_{3322} - \mathscr{T}_{1122}\mathscr{T}_{3333}), \quad \mathscr{T}_{1133}^{-1} = \frac{1}{\mathscr{D}}(\mathscr{T}_{1122}\mathscr{T}_{2233} - \mathscr{T}_{1133}\mathscr{T}_{2222}),$$

$$\tag{A.9}$$

$$\begin{aligned}\mathscr{D} = {}&\mathscr{T}_{2211}\mathscr{T}_{1133}\mathscr{T}_{3322} + \mathscr{T}_{2222}\mathscr{T}_{1111}\mathscr{T}_{3333} + \mathscr{T}_{1122}\mathscr{T}_{2233}\mathscr{T}_{3311} \\ &- \mathscr{T}_{1133}\mathscr{T}_{2222}\mathscr{T}_{3311} - \mathscr{T}_{2233}\mathscr{T}_{1111}\mathscr{T}_{3322} - \mathscr{T}_{2211}\mathscr{T}_{1122}\mathscr{T}_{3333},\end{aligned}$$

with all other non-zero components following by the cyclic permutation of $(1, 2, 3)$.

Precluding rigid-body rotation, formulas for the stress and displacement fields inside the defect can be found from (A.4)–(A.6) as

$$\boldsymbol{C}^\star : \nabla\overset{\star}{\boldsymbol{\vartheta}} = \boldsymbol{C}^\star : (\mathscr{S} : \mathscr{R} + \boldsymbol{D}) : \boldsymbol{\sigma}^\infty, \qquad \overset{\star}{\boldsymbol{\vartheta}} = [(\mathscr{S} : \mathscr{R} + \boldsymbol{D}) : \boldsymbol{\sigma}^\infty] \cdot \boldsymbol{\zeta}, \quad \boldsymbol{\zeta} \in \mathscr{B}. \tag{A.10}$$

With reference to (47), the first formula in (A.10) yields an explicit expression for the fourth-oder tensor $\mathscr{Q}$ in (54) for the case of an ellipsoidal inclusion as

$$\mathscr{Q}(\boldsymbol{m}) = \boldsymbol{C}^\star : (\mathscr{S} : \mathscr{R} + \boldsymbol{D}), \tag{A.11}$$

where $\mathscr{S}$ is again the Eshelby tensor and $\mathscr{R}$ is given by (A.6).

For the purpose of calculating the fourth-order tensor $\mathscr{V}(\boldsymbol{m})$ in (44), it is useful to note that

$$\mathscr{V} : \boldsymbol{\sigma}^\infty = \mathscr{V}_{ijkl}\,\sigma_{kl}^\infty\,\boldsymbol{e}_i \otimes \boldsymbol{e}_j = \frac{1}{|\mathscr{B}|}\int_{\partial\mathscr{B}}\tilde{\vartheta}_i(\boldsymbol{\zeta})\,\eta_j(\boldsymbol{\zeta})\,\mathrm{d}\mathscr{S}_\zeta = \frac{1}{|\mathscr{B}|}\int_{\partial\mathscr{B}}\tilde{\boldsymbol{\vartheta}} \otimes \boldsymbol{\eta}\,\mathrm{d}\mathscr{S}_\zeta. \tag{A.12}$$

Here $\boldsymbol{\eta}$ is the unit normal on $\partial\mathscr{B}$ oriented toward the interior of the defect, and $\tilde{\boldsymbol{\vartheta}}$ is the perturbation displacement field following (A.2) whose variation inside $\mathscr{B}$ can be calculated from (A.10) as

$$\tilde{\boldsymbol{\vartheta}}(\boldsymbol{\zeta}) = \overset{\star}{\boldsymbol{\vartheta}} - \boldsymbol{D} : \boldsymbol{\sigma}^\infty \cdot \boldsymbol{\zeta} = (\mathscr{S} : \mathscr{R} : \boldsymbol{\sigma}^\infty) \cdot \boldsymbol{\zeta}, \quad \boldsymbol{\zeta} \in \mathscr{B}. \tag{A.13}$$

To evaluate the last integral in (A.12), it is useful to introduce the (non-symmetrized) fourth-order identity tensor $\boldsymbol{\mathscr{I}}_4 = \delta_{ik}\delta_{jl}\boldsymbol{e}_i \otimes \boldsymbol{e}_j \otimes \boldsymbol{e}_k \otimes \boldsymbol{e}_l$. With such definition, one finds

using the divergence theorem and (A.13) that

$$\int_{\partial\mathcal{B}} \tilde{\boldsymbol{\vartheta}} \otimes \boldsymbol{\eta}\,\mathrm{d}\mathscr{S}_\zeta = \int_{\partial\mathcal{B}} (\tilde{\boldsymbol{\vartheta}} \cdot \boldsymbol{\mathcal{I}}_4) \cdot \boldsymbol{\eta}\,\mathrm{d}\mathscr{S}_\zeta = -\int_{\mathcal{B}} \overleftarrow{\nabla}\cdot(\tilde{\boldsymbol{\vartheta}} \cdot \boldsymbol{\mathcal{I}}_4)\,\mathrm{d}\mathcal{B}_\zeta = -|\mathcal{B}|\mathscr{S} : \mathscr{R} : \boldsymbol{\sigma}^\infty,$$

so that

$$\mathscr{V} : \boldsymbol{\sigma}^\infty = -\mathscr{S} : \mathscr{R} : \boldsymbol{\sigma}^\infty \quad\Longrightarrow\quad \mathscr{V}(\boldsymbol{m}) = -\mathscr{S} : \mathscr{R}; \tag{A.14}$$

a result that follows from (A.12), the fact that $\boldsymbol{\sigma}^\infty$ is an arbitrary (symmetric) second-order tensor, and the minor symmetries of $\mathscr{R}$. Finally, by recalling the formula

$$\mathscr{A}(\boldsymbol{m}) = \boldsymbol{D} : [\boldsymbol{I}_4 - \mathscr{Q}(\boldsymbol{m})] - \mathscr{V}(\boldsymbol{m}),$$

and employing (A.6), (A.11) and (A.14), it can be shown that

$$\mathscr{A}(\boldsymbol{m}) = \boldsymbol{D} : [\boldsymbol{I}_4 - \boldsymbol{C}^\star : (\mathscr{S} : \mathscr{R} + \boldsymbol{D})] + \mathscr{S} : \mathscr{R} \equiv \mathscr{R}. \tag{A.15}$$

References

Achenbach, J.D., 2003. Reciprocity in Elastodynamics. Cambridge University Press, Cambridge, UK.

Aki, K., Richards, P.G., 2002. Quantitative Seismology. University Science Books, Sausalito, CA.

Ammari, H., Kang, H., 2004. Reconstruction of the Small Inhomogeneities from Boundary Measurements. Springer, Berlin, New York.

Bonamy, D., Dalmas, D., Bouchaud, E., Guillot, C., 2005. Nano-ductile crack propagation in glasses under stress corrosion: spatiotemporal evolution of damage in the vicinity of the crack tip. Int. J. Solids Struct. 42, 637–645.

Bonnet, M., 1995. BIE and material differentiation applied to the formulation of obstacle inverse problems. Eng. Anal. with Bound. Elem. 15, 121–136.

Bonnet, M., 1995. Regularized BIE formulations for first- and second-order shape sensitivity of elastic fields. Comput. Struct. 56, 799–811.

Bonnet, M., 1999. Boundary Integral Equation Methods for Solids and Fluids. Wiley, New York.

Bonnet, M., Guzina, B.B., 2004. Sounding of finite solid bodies by way of topological derivative. Int. J. Num. Meth. Eng. 61, 2344–2373.

Colton, D., Kress, R., 1992. Inverse Acoustic and Electromagnetic Scattering Theory. Springer, Berlin.

Dahlquist, G., Bjorck, A., 1974. Numerical Methods. Prentice-Hall, Englewood Cliffs, NJ.

Eschenauer, H.A., Kobelev, V.V., Schumacher, A., 1994. Bubble method for topology and shape optimization of structures. Struct. Optim. 8, 42–51.

Eshelby, J.D., 1957. The determination of the elastic field of an ellipsoidal inclusion and related problems. Proc. Roy. Soc. London A 241, 376–396.

Fatemi, M., Greenleaf, J.F., 1998. Probing the dynamics of tissue at low frequencies with the radiation force of ultrasound. Phys. Med. Biol. 45, 1449–1464.

Gallego, R., Rus, G., 2004. Identification of cracks and cavities using the topological sensitivity boundary integral equation. Comp. Mech. 33, 154–163.

Garreau, S., Guillaume, P., Masmoudi, M., 2001. The topological asymptotic for PDE systems: the elasticity case. SIAM J. Control Optim. 39, 1756–1778.

Guzina, B.B., Bonnet, M., 2004. Topological derivative for the inverse scattering of elastic waves. Quart. J. Mech. Appl. Math. 57, 161–179.

Guzina, B.B., Chikichev, I., Scattering of elastic waves in a functionally-graded solid. ASME J. Appl. Mech. (in preparation).

Guzina, B.B., Pak, R.Y.S., 1996. Elastodynamic Green's functions for a smoothly heterogeneous half-space. Int. J. Solids Struct. 33, 1005–1021.

Guzina, B.B., Pak, R.Y.S., 2001. On the analysis of wave motions in a multi-layered solid. Quart. J. Mech. Appl. Math. 54 (1), 13–37.

Guzina, B.B., Nintcheu, S.F., Bonnet, M., 2003. On the stress-wave imaging of cavities in a semi-infinite solid. Int. J. Solids Struct. 40, 1505–1523.

Kellogg, O.D., 1954. Foundations of Potential Theory. Dover, New York, NY.

Kupradze, V.D., 1965. Potential Methods in the Theory of Elasticity. Israel Program for Scientific Translations, Jerusalem.

Madyarov, A.I., Guzina, B.B., 2006. A radiation condition for layered elastic media. J. Elasticity 82, 73–98.

Malvern, L.E., 1969. Introduction to the Mechanics of a Continuous Medium. Prentice-Hall, Englewood Cliffs, New Jersey.

Mazars, J., Pijaudier-Cabot, C., Saouridis, G., 1991. Size effect and continuous damage in cementitious materials. Int. J. Fract. 51, 159–173.

McLean, W., 2000. Strongly Elliptic Systems and Boundary Integral Equations. Cambridge University Press, Cambridge, UK.

Mura, T., 1987. Micromechanics of Defects in Solids. Martinus Nijhoff Publishers, Dordreght, Boston, Lancaster.

Pak, R.Y.S., Guzina, B.B., 1995. Three-dimensional wave propagation analysis of a smoothly heterogeneous solid. J. Mech. Phys. Solids 43, 533–551.

Pak, R.Y.S., Guzina, B.B., 1999. Seismic soil-structure interaction analysis by direct boundary element methods. Int. J. Solids Struct. 36, 4743–4766.

Plessix, R.E., De Roeck, Y.H., Chavent, G., 1998. Waveform inversion of reflection seismic data for kinematic parameters by local optimization. SIAM J. Sci. Comput. 20, 1033–1052.

Pommier, J., Samet, B., 2005. The topological asymptotic for the Helmholtz equation with Dirichlet condition on the boundary of an arbitrarily shaped hole. SIAM J. Control Optim. 43, 899–921.

Samet, B., Amstutz, S., Masmoudi, M., 2003. The topological asymptotic for the helmholtz equation. SIAM J. Control. Optim. 42, 1523–1544.

Samet, B., Amstutz, S., Masmoudi, M., 2004. The topological asymptotic for the Helmholtz equation. SIAM J. Control Optim. 42, 1523–1544.

Sarvazyan, A.P., Rudenko, O.P., Swanson, S.D., Fowlkes, J.B., Emelyanov, S.Y., 1998. Shear wave elasticity imaging: a new ultrasonic technology of medical diagnostics. Phys. Med. Biol. 24, 1419–1435.

Schroeder, C.T., Scott, W.R., Larson, G.D., 2002. Elastic waves interacting with buried land mines: a study using the FDTD method. IEEE Trans. Geosci. Remote Sensing 40, 1405–1415.

Sheriff, R.E., Geldart, L.P., 1995. Exploration Seismology. Cambridge University Press, Cambridge, UK.

Sokolowski, J., Zochowski, A., 1999. On the topological derivative in shape optimization. SIAM J. Control Optim. 37, 1251–1272.

Vladimirov, V.S., 1979. Generalized Functions in Mathematical Physics. Nauka, Moscow (in Russian).

Xu, X.H., 2004. Damage evaluation and damage localization of rock. Theor. Appl. Fract. Mech. 42, 131–138.